Journal of Aircraft, Available online 26 November 2025
DOI: 10.2514/1.c037996

Defect Force and Viscous Mechanical Energy Generation in Aerodynamic Flows

Ioannis Lamprakis* and Drewan S. Sanders†
Cranfield University,Cranfield, Bedfordshire, England MK430AL, United Kingdom

A defect integral analysis of the 2D compressible steady-state viscous flow about unpowered aerodynamic bodies is derived in this paper based on momentum and mechanical energy conservation. The defect flow field is obtained by subtracting the equivalent inviscid flow field from the real viscous flow, thereby retaining only entropy-related pertubations within boundary and free shear layers that contribute to viscous drag and mechanical loss generation. First, a defect momentum balance is derived that introduces the notion of the defect force, its farfield decomposition and its relation to the conventional viscous drag definition (profile drag minus wave drag). Next, a mechanical defect energy formulation is carried out in the relative reference frame that offers a means of explicitly and implicitly calculating the mechanical energy losses including, for the first time, compressibility-induced losses for both adiabatic and non-adiabatic flows. Finally, a defect mechanical formulation is derived in the absolute reference frame that provides an energy-based decomposition of the defect and conventional drag power into its mechanical energy loss and viscous excess mechanical energy constituents. The result is a clear identification and traceability of the evolution of viscosity-induced mechanisms related to viscous drag, mechanical energy loss generation and recoverable viscous mechanical energy, relevant for boundary layer ingestion propulsion. The formulations are numerically and experimentally advantageous because they only require integration across the shear layer height and all the momentum and mechanical energy terms can be implicitly calculated from surface integrations of readily available numerical and experimental data.

Nomenclature

a	=	angle of attack, deg
$C_{\mathcal{D}}, c_D, c_{\mathcal{F}_D}$	=	dissipation, nearfield viscous drag, defect drag coefficients
$D, \bar{D}$	=	drag, Aguirre's non-isentropic drag, N
$\mathcal{D}$	=	dissipation rate, W/m

*PhD Student, School of Aerospace,Transport and Manufacturing, ioannis.lamprakis@cranfield.ac.uk
†Lecturer, School of Aerospace,Transport and Manufacturing, d.s.sanders@cranfield.ac.uk.

Published by AIAA. This is the Author Accepted Manuscript issued with: Creative Commons Attribution License (CC:BY 4.0).
The final published version (version of record) is available online at DOI:10.2514/1.c037996. Please refer to any applicable publisher terms of use.

$d\mathcal{S}$	=	infinitesimal surface element of control volume, m^2
$d\mathcal{V}$	=	infinitesimal volume element of control volume, m^3
e	=	mass specific internal energy, J/kg
f_x	=	body force per unit volume in the x-direction, N/m^3
$\boldsymbol{\mathcal{F}}, \boldsymbol{\mathcal{F}}_p, \boldsymbol{\mathcal{F}}_v$	=	defect force, defect pressure force and friction force vectors, N
$\mathcal{F}_D, \mathcal{F}_\mathcal{L}$	=	defect drag, defect lift components, N
M	=	Mach number
$\boldsymbol{\mathcal{M}}$	=	momentum defect flux vector, N
$\mathbf{M}$	=	mass defect vector, $kg/(s \cdot m)$
$\hat{\boldsymbol{n}}$	=	unit normal vector
p, p^*, p_G, P_t	=	static, (Aguirre's) isentropic static, gauge static and total pressures, Pa
$\boldsymbol{\mathcal{P}}$	=	pressure defect flux vector, N
Pr	=	Prandtl number
$\mathcal{PER}$	=	potential for energy recovery
r	=	temperature recovery factor
$\boldsymbol{Q}$	=	volume-flux defect vector, m^3/s
Re_c	=	$\rho_\infty V_\infty c/\mu_\infty$, chords-based Reynolds number
Re_θ	=	$\rho_e V_e \theta/\mu_\infty$, mom. thickness-based Reynolds number
s, n	=	local coordinate system
s	=	mass specific entropy, $J/K/kg$
$\mathcal{S}$	=	control volume surface, m^2
T, T_t	=	static, total temperatures, K
$\boldsymbol{\mathcal{T}}$	=	viscous stress force vector, N
T_w	=	wall static temperature, K
u, v, w	=	absolute velocity components, m/s
$\mathcal{V}$	=	control volume, m^3
$\mathbf{V}, \mathbf{V}^*, \bar{\mathbf{V}}$	=	fluid velocity vector, (Aguirre's) isentropic and non-isentropic velocity vectors, m/s
$\mathbf{V}_\mathrm{A}$	=	$\mathbf{V} - \mathbf{V}_\infty$ absolute reference frame fluid velocity vector, m/s
α	=	speed of sound, m/s
γ	=	specific heat ratio
$\delta, \delta^*, \delta^{**}, \delta_k$	=	boundary layer, displacement, density-flux and volume-flux thicknesses, m
Δ^*, Δ^{**}	=	displacement (mass-defect), density-flux defect areas, m^2

$\dot{\mathcal{E}}_{\mathcal{K}}, \dot{\mathcal{E}}_{\mathcal{K}}, \dot{\mathcal{E}}_{\tau}$ = kinetic energy defect, pressure-work defect and viscous boundary work rates, W

$\widetilde{\mathcal{E}}_k, \widetilde{\mathcal{E}}_p, \widetilde{\mathcal{E}}_{\tau}$ = viscous kinetic energy excess, viscous pressure-work and viscous boundary work rates, W

$\bar{\tilde{\mathcal{E}}}_k, \bar{\tilde{\mathcal{E}}}_p$ = Aguirre's non-isentropic kinetic energy and pressure boundary work rates, W

$\dot{\mathcal{E}}$ = $\dot{\mathcal{E}}_k + \dot{\mathcal{E}}_p + \dot{\mathcal{E}}_{\tau}$, mechanical energy/exergy outflow rate, W

ζ = isentropic parameter

Θ = volumetric pressure work rate, W or mom. defect area (for boundary layer analysis), m^2

$\Theta_r, \mathcal{B}, \Theta_{\infty}$ = reversible, baroclinic, residual volumetric pressure work rate, W

$\mathbf{K}^*, \mathbf{K}$ = kinetic energy defect, wake kinetic energy excess, $kg/(s \cdot m)$

ξ = boundary layer identifier

$-\Pi_V$ = Sato's baroclinic power term, W

ρ = density, kg/m^3

$\bar{\bar{\tau}}$ = viscous stress tensor, Pa

Φ = viscous dissipation rate, W

Φ^* = $\Phi + \mathcal{B}$, total mechanical losses, W

Subscripts

∞ = freestream-quantity

A = absolute reference frame quantity

B, = quantity on body and equivalent inviscid body surface

BL = boundary layer quantity

e = boundary layer edge quantity

FP = flat plate quantity

i = equivalent inviscid flow quantity

TE = trailing edge quantity

TP = Trefftz plane quantity

wake = wake quantity

I. Introduction

Numerous farfield methods have been developed to predict the drag force of an aerodynamic body and decompose it into contributions from flow mechanisms such as shear layers, vortical systems and shockwaves.These methods typically build upon the earlier work by Oswatitsch [1] and rely on 2^{nd} Law thermodynamics and mathematical manipulations (Taylor series expansion, higher order term omission) to express the viscous and shock wave drag components as a

function of entropy and enthalpy changes [2–6]. For 3D lifting flows, the remaining induced drag component is then obtained via a Trefftz plane integration of the transverse kinetic energy [2, 3, 7–9]. The validity of both the induced drag definition and the integration plane convention have been questioned by Spalart [10] as being ambiguous even for light loading conditions of negligible vortex roll-up. The apparent lack of a rigorous lift-induced drag definition and the need for a phenomenological breakdown of lift have been addressed by the vortex force theory, initially proposed by Wu et al. [11] for incompressible unsteady flow and further extended for high Reynolds number, steady state, compressible flows [12–15]. The claimed benefits of the lamb-vector-based breakdown include, amonst others, unambiguous definitions of lift and lift-induced drag [13], removal of spurious contributions due to targeted integrations across regions of finite vorticity [14] and distinction between "reversible" (related to lift and lift-induced drag) and "irreversible" (related to profile drag) force components [15, 16].

It should be noted that the appellations "reversible" and "irreversible", as traditionally used in momentum-based methods, are labeling conventions and do not necessarily imply an ability to extract irreversibilities from the flow field. The latter requires an examination of the power transfer mechanisms from the aerodynamic body to the flow. This has been demonstrated by Drela [17] via a power balance based on mechanical energy conservation. From an energy perspective, the drag power of an unpowered aerodynamic body is decomposed into physically intuitive power sink and power sources, with the former accounting for "irreversible" energy conversion into heat and the latter for the recoverable (and thus not irreversible) energy portion that could, for example, be utilized by a Boundary Layer Ingestion (BLI) propulsor. Sanders and Laskaridis [18] have provided an elegant and more intuitive interpretation of the power transmission mechanisms from the airframe surfaces to the flow by demonstrating that the power balance effectively corresponds to an Absolute Reference Frame (ARF) formulation, where the aerodynamic body is flying through quiescent atmosphere. The same authors introduced a potential for energy recovery (PER) factor to explicitly assess the portion of the drag power that could be recovered for improved aerodynamic performance, with a modified compressibility-corrected formulation being proposed thereafter by Lamprakis et al. [19].

The capabilities of energy-based methods in assessing the aerodynamic performance of both unpowered and powered configurations have been verified both numerically and experimentally in various studies [18–24], however, they retain the inherent limitation of conventional control volume approaches: The inability to define and correlate local force generation with mechanical energy loss and excess production mechanisms associated with the airframe surfaces. To further elaborate, consider a 2D subsonic adiabatic viscous flow about an aerodynamic body. For this scenario, the total drag is the by-product of the friction forces (skin friction drag) and the partial self-cancellation* of the pressure field (pressure drag) due to the viscous displacement effect of the boundary layer [5]. The force integration is meaningful only for the fully enclosed aerodynamic body. Attempting to carry out a similar momentum or power balance analysis over a part of the airfoil is bound to be futile because of the "unbalanced" isentropic pressure forces associated with

*In the absence of shockwaves, the nearfield pressure field integration of a 2D inviscid flow field self-cancels perfectly.

the precluded body surfaces. The same applies for the corresponding inviscid flow scenario where the evolution of momentum and power balance terms would involve non-zero contributions along the body surfaces that only cancel out perfectly downstream of the trailing edge, yielding zero drag. This counter-intuitive result seems to suggest that partial body surfaces yield a finite force and therefore a locally finite power trace that only self-cancels for the fully enclosed body. These force and power pertubations are, however, "pseudo-contributions" of the isentropic-flow field rather than a corollary of actual viscous power transfer mechanisms from the body to the flow that contribute to drag. As such, the evolution of drag production and its subsequent energy-based manifestation are traceable and well defined only to the extent that isentropic "pseudo-contributions" are sifted out from the flow field.

The idea of filtering isentropic contributions is implicitly utilized for farfield drag estimation purposes by positioning the downstream Trefftz plane along the fully-expanded wake region where the shear layer flow is decoupled from the pressure field of the aerodynamic body. This enables drag estimations from the integration of the momentum defect within the shear layer height rather than the entire Trefftz plane, but does not resolve any of the aforementioned challenges. In the limiting scenario of a zero-pressure gradient flat plate flow, however, the absence of a pertubation pressure field enables direct causality between flow field pertubations and viscosity-induced effects (via the no slip condition). For this flow scenario, the drag generation process is well-defined and measured by the integrated skin friction force whereas the affiliated power transfer mechanisms by the sum of the upstream dissipation and excess kinetic energy [17]. Also notice that for an inviscid flat plate flow, the absence of pseudo-work/force contributions yields locally the expected zero force and power traces, in agreement with the zero drag result of the fully enclosed flat plate. In that sense, the power balance may be meaningfully applied along partial flat plate surfaces to establish a causal relation between local (skin friction) force production and its energy-based manifestation. Such an analysis has been carried out by Renard and Deck [25] via a mechanical energy budget in the ARF, where the flat plate is moving through undisturbed atmosphere, in order to decompose the local skin friction generation into physical phenomena. However, the derived energy-budget stems from the conventional real viscous flow (RVF) (the formulation coincides with power balance [25]) and its validity along wall surfaces is "coincidental" and physically meaningful only for the flat plate scenario. Similar limitations apply to the PER definition [18, 19] of unpowered bodies in that the RVF power balance provides an estimate of the mechanical energy excess deposited to the wake, but no information about the physical processes associated with its upstream generation from the body's surfaces. For compressible flows, the quantification of PER in the near wake region involves a degree of arbitrariness due to the non-negligible isentropic energy transfers between the mechanical energy outflow and the volumetric pressure power term. The interpretation and estimation of the latter has been a rather enigmatic and challenging task and its incorporation within the balance is typically omitted or vaguely accounted for via a dissipation correction [20, 22] based on previous results by Sato [26].

Sato [26] demonstrated how pseudo-work contributions may be (approximately) filtered out by carrying out a decomposition of the RVF into two components: The equivalent inviscid flow (EIF) about the effective body due

to the additional viscous displacement effect [27] and the defect viscous flow field (DVF) that accounts for viscous (profile) losses due to boundary and free shear layers. Sato then formulated a mechanical energy defect balance in the Relative Reference Frame (RRF) based on Thin Shear Layer (TSL) approximations that enabled, for the first time, the identification and estimation of the baroclinic [26] component (typically losses) of the volumetric pressure power term. It could be argued that the notion of defect quantities is well-understood as being an inherent part of integral boundary layer relations (momentum or kinetic energy) [28–30] however the latter stem from the RVF whereas the EIF concept[†] is utilized for the viscous-inviscid coupling of BL codes such as XFOIL and MSES [28, 29]. Previous momentum-based farfield approaches have coincidentally touched upon the defect DVF concept by addressing the wake's streamwise defect (or pertubation) velocity using thermodynamic relations [2, 8, 32] but only as a means of reducing the integration plane for the profile drag estimation. A promising idea on the topic involves the decomposition of the pressure field into Euler (inviscid) and dissipative (viscous) partial pressure field as suggested by Schmitz and Coder [33] initially for incompressible flow and for compressible flow [34] thereafter. The inviscid partial pressure field is shown to relate to a corrected Kutta-Joukowski lift theorem, Maskell's vortex induced drag expression, including the debatable $-u^2$ term addressed by Spalart [10] and Drela [17], while the latter to viscosity-induced entropy flux correlation of Oswatitsch. However, the decomposition has only been carried out within the context of force measurements rather than energy-based quantities. Its numerical implementation is also non-straightforward as Poisson solvers are required for the breakdown of the pressure fields. A more intuitive and relevant approach (for the purposes of this study) on the removal of the isentropic flow field has been proposed recently by Aguirre [35] and Aguirre et al. [36] via a wake-plane reduced exergy formulation from the initial RVF exergy balance of Arntz [37, 38]. This was achieved by extending Meheut's [32] isentropic and non-isentropic velocity pertubation breakdown based, however, on wrongly perceived inviscid flow definitions (to be discussed later) to approximately filter out the entire isentropic flow field. The robustness and consistency of the formulation was subsequently tested and verified in various flow scenarios (2D and 3d lifting) under the narrow prism however of an exergy-based, wind-tunnel adapted far field drag estimation method rather than as a comprehensive means of understanding and addressing causality between local force (drag) generation and its viscous power manifestation.

In light of the above, the present paper aims to build upon the previous work by Sato [26] and Aguirre [36] by formally and rigorously deriving the conservation form of the governing defect momentum and mechanical energy relations from first principles. Boundary layer assumptions will be invoked in the subsequent derivations, which are valid for high Reynolds number flows. Therefore, the formulations lose accuracy, locally, in regions with strong adverse pressure gradients or flow separation. The paper is structured in self-contained but interconnected sections where the underlying theory is supplemented with RANS-CFD results of adiabatic and non-adiabatic NACA0012 airfoil studies. First, the concepts of the EIF and DVF are introduced, including necessary derivation assumptions and control volume

[†]A detailed analysis of EIF modelling techniques is provided by Drela [27, 31])

definitions. Next, the defect momentum equation is derived to introduce the notion of the defect force as a measure of local profile drag generation and its causal relation to conventional profile drag is discussed. A defect mechanical energy balance is subsequently derived in the RRF that offers a means of tracing and quantifying the mechanical loss production mechanisms along the airframe and the walls, including, for the first time, thermo-compressibility induced losses and their affiliation with Sato's [26] baroclinic power is addressed. Finally, the defect mechanical energy is derived in the ARF correlating, for the first time, local defect drag production with entropic viscous power transfer/productions mechanisms which are numerically shown to be closely linked to energy recovery via BLI propulsion.

II. Defect Flow Field Definitions

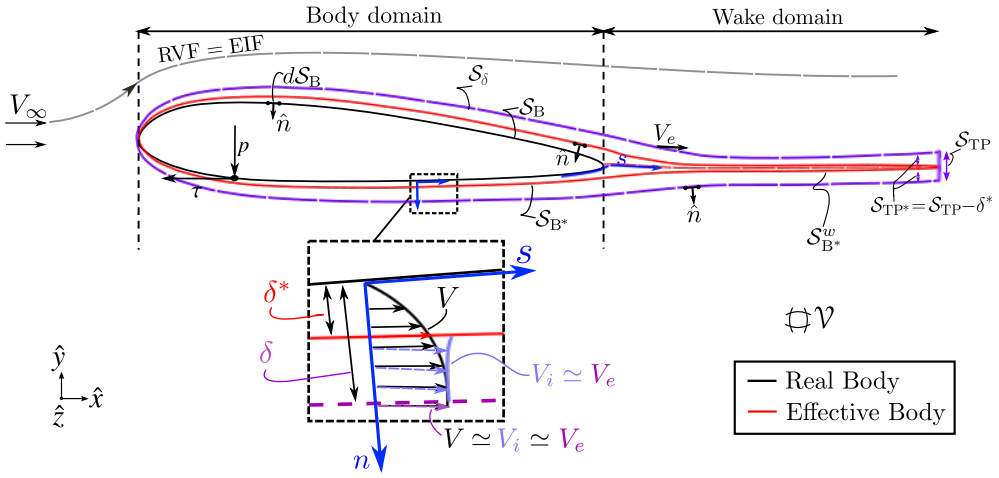


Fig. 1 Superpositioned real viscous flow and equivalent inviscid flow fields over the real and effective (inviscid) aerodynamic bodies, along with annotated control volume definitions and relevant flow features.

A. Equivalent Inviscid Flow

Consider the Real Viscous Flow (RVF) forming over an arbitrary aerodynamic body, as shown in Fig. 1. The viscous motion of the fluid partitions the aerodynamic domain into a viscous and an inviscid region. The viscous region encloses the shear layers, delimited by the body's surfaces $\mathcal{S}_\mathrm{B}$ and the local shear layer thickness δ, that defines the outer viscous-inviscid interface (edge) $\mathcal{S}_\delta$ along the body and the wake domains. The inviscid region encloses the outer irrotational flow field associated with potential bulk flow pertubations that naturally self recover to free-stream conditions downstream. Relative to a purely inviscid flow, the outer potential flow field structure of the RVF is determined by the effective aerodynamic displacement imposed by the wall curvature as well as the viscous deflection of the flow. That is, the outer flow is imposed by a "fictitious" or Effective Inviscid Body (EIB) that deviates locally from the real by a wall-normal distance equal to the displacement thickness, δ^*, of the shear layer and extends to the wake, as illustrated in Fig. 1 (red lines).

For non-lifting flows, the wake displacement shape is merely symmetrically displaced about the chord line, while additional conditions (zero pressure jump or velocity jump requirement [27] are required to fully determine the wake camber shape of lifting flows. For bodies with sharp trailing edge, the wake shape of the EIB is determined by the flow streamline emanating from the trailing edge that separates the upper and lower wake portions. From the above, the Equivalent Inviscid Flow (EIF) may be defined as the inviscid flow that replicates the same outer inviscid flow field conditions as that of the corresponding RVF. The physical requirement is satisfied by imposing vertical (wall-normal) mass flux matching between the EIF and the RVF outside the assumed viscous/inviscid interface, $\mathcal{S}_\delta$, thereby accounting for the shear layer's mass defect. Drela [27, 29] has shown that the EIF may be constructed by simply considering the invsicid flow over the corresponding EIB or alternatively by a wall transpiration model.

In the subsequent sections, all EIF quantities will be denoted with the subscript $()_i$, shear layer edge quantities with the subscript $()_e$ while flow field variables without subscripts will refer to RVF. For further derivation purposes, the flow field analysis will be carried out with respect to the local Cartesian $s-n$ coordinate system, with the s, n axes being, respectively, tangent and normal to the local curvature of the real body and the effective camber line of the EIB in the wake.

B. Defect Flow Field

Consider the velocity profiles of the RVF and EIF, shown in Fig. 1 (zoomed region), at an arbitrary position, s, along the real and the effective body, respectively. The RVF yields a boundary layer profile $V(n)$ that initiates at the wall ($n = 0$) and propagates up to the shear layer edge ($n = \delta$) where $V = V_e$. At the same position, the corresponding EIF forms a nearly uniform inviscid velocity distribution, $V_i(n)$, that is tangent to the local curvature of the EIB ($n = \delta^*$) and is delimited by the same outer edge boundary, $n = \delta$ with $V_i \approx V_e$. The streamlines of the two flows are generally misaligned due to local curvature deviation between the real and effective wall orientations, while the additional viscous self-deflection of the boundary layer partially acts towards mitigating the relative streamline divergence. That is, shear layer velocity vectors farther from the wall are experiencing larger "accumulated" viscous self-deflection and eventually align with the EIF at the outer edge boundary, as illustrated in Fig. 1. Noting that the outer potential flow field is the same for both flows, the EIF measures the isentropic pertubations of the shear layer, thereby allowing for the notional decomposition of the RVF into its isentropic (EIF) and entropic constituents, the latter being the defect viscous flow (DVF), defined conceptually as:

$$\text{DVF} = \text{RVF} - \text{EIF} \tag{1}$$

The definition (1) of the defect flow is demonstrated in Fig. 2 in terms of the defect velocity profile which follows from the RVF by shifting out the respective isentropic contributions inside the shear layer. Thereby, a defect integral analysis of the flow field offers a unique means of establishing causal relation between flow field pertubations affiliated with

profile loss mechanisms inside shear layers.

C. Assumptions

In simplifying the subsequent derivations, it will be assumed, similar to Sato [26], that the flow field properties of the EIF are nearly uniform normal to the wall and are imposed by the outer potential flow, such that:

$$()_i \approx ()_e \tag{2}$$

A similar approximation for the pressure variation, i.e., $p \approx p_e$, of the RVF shear layer may be invoked from the thin shear layer approximation. However, this assumption is not required nor implied throughout, unless explicitly mentioned. The vertical (wall-normal) velocity component V_n of the RVF is assumed negligible, such that the velocity vector is parallel to the wall, i.e., $V \simeq V_s$. Additionally, the misalignment of the streamlines between the RVF and the EIF is also neglected, as per Sato [26], whereas similar approximations have been adopted by Aguirre [35] and Aguirre et al. [36]. It should be noted that this assumption strictly holds for high Reynolds number flows, where the vertical offset of the EIF streamlines relative to the RVF is negligible. For lower Reynolds number flows, or in regions of the aerodynamic body with significant adverse pressure gradients (such as the aft part of an airfoil) or separation, the viscous displacement (δ^*) becomes more pronounced, and the accuracy of the approximation locally diminishes. The principles of the defect flow will be initially addressed from the Relative Reference Frame (RRF) perspective, i.e., for a stationary aerodynamic body with the flow passing over it. However, its applicability will be shown to extend to the Absolute Reference Frame (ARF), where the aircraft is flying through quiescent atmosphere, providing a means of measuring the viscous energy transmission mechanisms from the body to the flow.

D. Defect Control Volume Definition

The defect integral analysis is carried over two continuous Control Volumes (CV) corresponding to the RVF and EIF, respectively. The former surrounds the actual aerodynamic body surfaces $\mathcal{S}_\mathrm{B}$ while the latter the fictitious inviscid body $\mathcal{S}_{\mathrm{B}^*}$ extending to the wake, as shown in Fig. 2 (upper). The positioning of the far-field boundaries for the RVF and EIF control volumes is unique and may not be freely chosen as in conventional farfield methods. The reason is that any flow perturbation outside the shear layers cancels out by definition. Therefore, the farfield control surface of the two CV consists of a shared defect outer boundary portion lying along the viscous/inviscid interface $\mathcal{S}_\delta$ and a Trefftz plane portion $\mathcal{S}_\mathrm{TP}$ positioned at an arbitrary position s along the flow path (including wall surfaces). Notice that the EIF crosses an "effective" Trefftz plane $\mathcal{S}_{\mathrm{TP}^*}$ only, due to the displacement of the EIB. With reference to Fig. 1, the RVF CV is defined as $\mathcal{S}_\mathrm{B} \cup \mathcal{S}_\delta \cup \mathcal{S}_\mathrm{TP}$, whereas the EIF as $\mathcal{S}_{\mathrm{B}^*} \cup \mathcal{S}_{\delta^*} \cup \mathcal{S}^*_\mathrm{TP}$ along the body domain or $\mathcal{S}_{\mathrm{B}^*} \cup \mathcal{S}^\mathrm{wake}_{\mathrm{B}^*} \cup \mathcal{S}_{\delta^*} \cup \mathcal{S}_{\mathrm{TP}^*}$ along the wake.

For further derivation purposes, the Trefftz plane will be oriented normal to wall surfaces when the CV partially encloses the body, and normal to the camber shape of the effective body for a fully enclosed configuration. All the control boundaries are closed with the elementary local surface element surface vector, $\hat{\boldsymbol{n}}$, pointing outwards in the farfield boundaries and inwards along the real and fictitious body surfaces. The Gauss's theorem will be extensively used in the following derivations to relate volume integral quantities to flux terms across the control surfaces:

$$\iiint \nabla \cdot () \, d\mathcal{V} = \oiint () \cdot \hat{\boldsymbol{n}} \, d\mathcal{S} \tag{3}$$

where () any vector field quantity. Invoking the identity (3) over the control volume of the RVF and EIF yields, respectively:

$$\iiint \nabla \cdot () \, d\mathcal{V} = \iint () \cdot \hat{\boldsymbol{n}} \, d\mathcal{S}_{\mathrm{B}} + \iint () \cdot \hat{\boldsymbol{n}} \, d\mathcal{S}_{\delta} + \iint () \cdot \hat{\boldsymbol{n}} \, d\mathcal{S}_{\mathrm{TP}} \tag{4}$$

$$\iiint \nabla \cdot () \, d\mathcal{V} = \iint () \cdot \hat{\boldsymbol{n}} \, d\mathcal{S}_{\mathrm{B}^*} + \iint () \cdot \hat{\boldsymbol{n}} \, d\mathcal{S}_{\delta} + \iint () \cdot \hat{\boldsymbol{n}} \, d\mathcal{S}_{\mathrm{TP}^*} \tag{5}$$

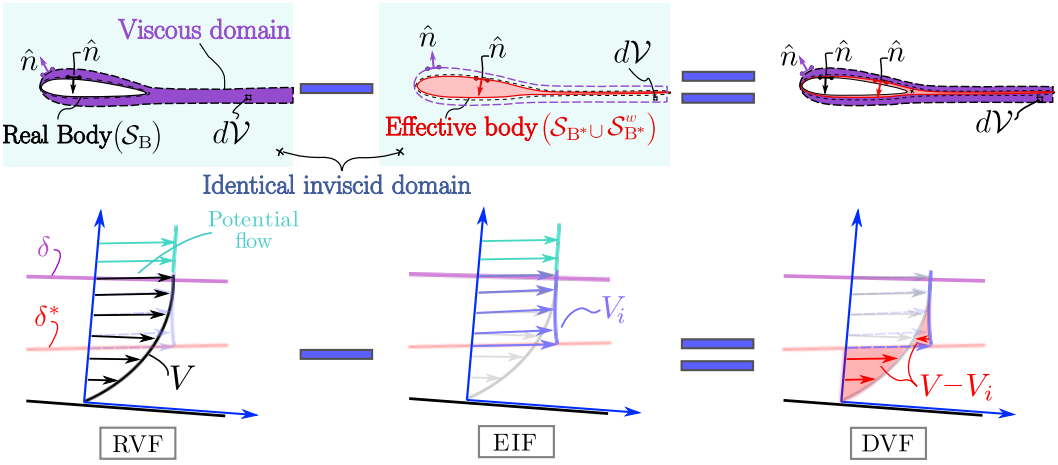


Fig. 2 RVF, EIF and DVF control volume definitions (upper) and corresponding velocity profiles (lower).

E. Defect Continuity Equation

The divergence form of the Reynolds-averaged steady state continuity equation is given by:

$$\nabla \cdot (\rho \boldsymbol{V}) = 0 \tag{6}$$

where ρ, the fluid density, and $\boldsymbol{V}$, the local velocity vector. The defect continuity relation is then obtained as the difference between the real and equivalent inviscid flow continuity relations:

$$\nabla \cdot (\rho_e \boldsymbol{V}_e) - \nabla \cdot (\rho \boldsymbol{V}) = 0 \tag{7}$$

The integral defect continuity relation follows from the volume integration of (7) along with the Gauss's identities (4), (5) as:

$$\iint [\rho_e \boldsymbol{V}_e - \rho \boldsymbol{V}] \cdot \hat{\boldsymbol{n}} \, d\mathcal{S}_{\mathrm{TP}} - \iint \rho_e \boldsymbol{V}_e \cdot \hat{\boldsymbol{n}} \, d\mathcal{S}_{\mathrm{TP}}^{\delta^*} = 0 \tag{8}$$

where $\mathcal{S}_{\mathrm{TP}}^{\delta^*}$ the portion of the Trefftz plane that initiates at $n = 0$ and extends up to $n = \delta^*$. Wall-related fluxes are zero due to the no-slip condition, $\boldsymbol{V} \cdot \hat{\boldsymbol{n}} \, d\mathcal{S}_{\mathrm{B}} = 0$, and due to the velocity vector ($\boldsymbol{V}_e$) being locally perpendicular to the surface direction vector, $\boldsymbol{V}_e \cdot \hat{\boldsymbol{n}} \, d\mathcal{S}_{\mathrm{B}^*}^{w} = 0$ for the RVF and EIF, respectively. Mass flux terms crossing the viscous/inviscid boundary $\mathcal{S}_\delta$ are also, by definition, equal for both flows and cancel out, so that the entire mass-defect flow is measured via the Trefftz plane defect. Equation (8) will be invoked in the following sections for simplification purposes.

F. Useful Remarks

All the subsequent formulations are complemented by numerical studies of adiabatic and non-adiabatic 2D NACA0012 airfoil at various operating conditions. A single test case of an axisymmetric BLI-powered fuselage is examined at the end of Section V, highlighting the correlation between the defect flow and energy recovery mechanisms. All the details about the numerical extraction of the viscous domain, the numerical setup, and useful shear layer properties are summarized in Appendices A, B and C, respectively.

III. Defect Momentum Equation

A. Formulation

The divergence form of the steady-state Reynolds-averaged momentum equation assuming negligible body forces is given by:

$$\nabla \cdot (\rho \boldsymbol{V}\boldsymbol{V}) = -\nabla p + \nabla \cdot \bar{\bar{\tau}} \tag{9}$$

where p denotes the static pressure of the fluid and $\bar{\bar{\tau}}$ the viscous stress tensor. The corresponding momentum defect relation is obtained as:

$$\nabla \cdot (\rho \boldsymbol{V}_e \boldsymbol{V}_e) - \nabla \cdot (\rho \boldsymbol{V}\boldsymbol{V}) = -\nabla p_e - [-\nabla p + \nabla \cdot \bar{\bar{\tau}}] \tag{10}$$

Volume integration of (9) along with the identities (4), (5) yields the following integral form:

$$\oiint \boldsymbol{V}_e \rho_e \boldsymbol{V}_e \cdot \hat{\boldsymbol{n}}\, d\mathcal{S}^* - \oiint \boldsymbol{V} \rho \boldsymbol{V} \cdot \hat{\boldsymbol{n}}\, d\mathcal{S} = - \oiint p_{G_e} \hat{\boldsymbol{n}}\, d\mathcal{S}^* - \oiint [-p_G \hat{\boldsymbol{n}} + \bar{\bar{\boldsymbol{\tau}}} \cdot \hat{\boldsymbol{n}}]\, d\mathcal{S} \tag{11}$$

where the substitution of the gauge pressure $p_G \rightarrow p - p_\infty$ is permissible because the RVF and EIF CV boundaries are closed. Invoking the defect continuity relation (8) and the approximation $V_i(n) \simeq V_e$ as per Eq. (2) for a given Trefftz plane normal to the wall, the left-hand side momentum flux integrals may be reduced to a single Trefftz plane momentum defect term:

$$\begin{aligned}
\oiint \boldsymbol{V}_e \rho_e \boldsymbol{V}_e \cdot \hat{\boldsymbol{n}}\, d\mathcal{S}^* - \oiint \boldsymbol{V} \rho \boldsymbol{V} \cdot \hat{\boldsymbol{n}}\, d\mathcal{S} = & \\
& \iint (\boldsymbol{V}_e \rho_e \boldsymbol{V}_e - \boldsymbol{V} \rho \boldsymbol{V}) \cdot \hat{\boldsymbol{n}}\, d\mathcal{S}_{\mathrm{TP}} - \iint \boldsymbol{V}_e \rho_e \boldsymbol{V}_e \cdot \hat{\boldsymbol{n}}\, d\mathcal{S}_{\mathrm{TP}}^{\delta^*} \\
& = \iint \left[\boldsymbol{V}_e \rho_e \boldsymbol{V}_e - \left(\boldsymbol{V}_e \rho_e \boldsymbol{V}_e - (\boldsymbol{V}_e - \boldsymbol{V}) \rho \boldsymbol{V} \right) \right] \cdot \hat{\boldsymbol{n}}\, d\mathcal{S}_{\mathrm{TP}} \\
& + \underbrace{\boldsymbol{V}_e \left(\iint (\rho_e \boldsymbol{V}_e - \rho \boldsymbol{V}) \cdot \hat{\boldsymbol{n}}\, d\mathcal{S}_{\mathrm{TP}} - \iint \rho_e \boldsymbol{V}_e \cdot \hat{\boldsymbol{n}}\, d\mathcal{S}_{\mathrm{TP}}^{\delta^*} \right)}_{=0} \\
& = \iint (\boldsymbol{V}_e - \boldsymbol{V}) \rho \boldsymbol{V} \cdot \hat{\boldsymbol{n}}\, d\mathcal{S}_{\mathrm{TP}}
\end{aligned} \tag{12}$$

where wall-related momentum-flux contributions as well as defect fluxes across the viscous/inviscid interface are zero, so that the entire momentum defect outflow is exiting from the Trefftz plane only. Substitution of (12) into (11) and expansion of the right-hand side terms yields the integral defect momentum equation which governs the defect aerodynamic force evolution along the flow path:

$$\boldsymbol{\mathcal{F}} = \boldsymbol{\mathcal{M}} + \boldsymbol{\mathcal{P}} + \boldsymbol{\mathcal{T}} \tag{13}$$

The left hand side equality of (13) represents the nearfield defect force vector while the right hand side its farfield manifestation. All terms are defined hereafter:

The defect force vector,

$$\boldsymbol{\mathcal{F}} = \underbrace{- \iint \bar{\bar{\tau}} \cdot \hat{\boldsymbol{n}}\, d\mathcal{S}_B}_{\boldsymbol{\mathcal{F}}_v} + \underbrace{\iint p_G\, \hat{\boldsymbol{n}}\, d\mathcal{S}_B - \iint p_{G_e}\, \hat{\boldsymbol{n}}\, d\mathcal{S}_{B^*}}_{\boldsymbol{\mathcal{F}}_p} \tag{14}$$

This term measures the nearfield defect aerodynamic force evolution along the flow path as the sum of the integrated friction force component $\boldsymbol{\mathcal{F}}_v$ and the pressure defect force $\boldsymbol{\mathcal{F}}_p$. The former coincides with the conventional RVF integrated skin friction force vector, which yields, for a fully enclosed body, the skin friction drag D_f and a marginal

defect-induced lift component in the streamwise and perpendicular flow directions, respectively. $\mathcal{F}_p$ describes, in the streamwise direction, the nearfield mechanism of pressure defect drag generation, as the integrated pressure force difference over the real and the fictitious bodies. In the lift direction, the pressure defect force component accounts for a marginal variation of lift distribution relative to the EIF due to weak, viscous-induced pressure field alterations. Comparison of $\mathcal{F}_v$ and $\mathcal{F}_p$ definitions underlines the fundamental difference between pressure and viscous force generation. The viscous forces are generated exclusively along the body's surfaces via the no-slip condition and viscosity, while the pressure defect force generation extends to the wake and runs (approximately) to completion when the camber shape of the EIB becomes parallel to the direction of the free-stream velocity. Notice that in practice, the (numerical) calculation of Eq. (14) is impractical, as it requires post-processing of both the RVF and corresponding EIF solutions. Therefore, its right-hand side decomposition will be used hereafter.

The momentum defect flux vector,

$$\mathcal{M} = \iint (\boldsymbol{V}_e - \boldsymbol{V})\rho \boldsymbol{V} \cdot \hat{\boldsymbol{n}}\, d\mathcal{S}_{\mathrm{TP}} \tag{15}$$

This is the integrated momentum flux defect flow crossing the Trefftz plane and measures the momentum deficit of the RVF relative to the EIF. For a 2D flow, this term reduces to conventional momentum defect $\rho_e V_e^2 \theta$ that appears (in non-dimensional form) in integral boundary layer formulations (see Drela and Giles [28], Drela [31] and Fidkowski [30]) as a convenient means of farfield drag extraction from wake plane measurements.

The pressure defect force vector,

$$\mathcal{P} = \iint (p_e - p)\hat{\boldsymbol{n}}\, d\mathcal{S}_{\mathrm{TP}} - \iint p_{G_e} \hat{\boldsymbol{n}}\, d\mathcal{S}_{\mathrm{TP}}^{\delta^*} \tag{16}$$

This is the integrated pressure force acting on the Trefftz plane due to the pressure distribution inside the shear layers deviating from the EIF. This term yields large positive contributions along flow regions of excess acceleration and negative contributions that balance large momentum defect fluxes along regions of strong adverse pressure gradients due to the thickening of the EIB.

The viscous stress force vector,

$$\mathcal{T} = \iint \bar{\bar{\boldsymbol{\tau}}} \cdot \hat{\boldsymbol{n}}\, d\mathcal{S}_{\mathrm{TP}} \tag{17}$$

This is the shear stress force acting on the Trefftz plane with locally marginal contributions that rapidly decay along the wake, where the velocity gradients progressively flatten out due to the action of viscosity. It may however be advantageous to retain this term for Trefftz planes positioned along wall surfaces and in the near wake region.

B. Defect Force Characterisation

The evolution of the defect force vector $\mathcal{F}$ (per unit span) acting on various Trefftz plane positions and the wake of an arbitrary 2D body at an angle of attack (AoA) a is shown qualitatively in Fig. 3. From the right-hand side of the

defect force balance Eq. (13), it follows that the sum of the defect components (their magnitude) $\mathcal{M} + \mathcal{P} + \mathcal{T}$ exerted on the Trefftz plane measures the total upstream nearfield defect force generation in the s - direction of the local $s-n$ coordinate system. The magnitude of the generated defect force $\mathcal{F} = \boldsymbol{\mathcal{F}} \cdot \hat{s}$ monotonically accumulates along the airfoil as it progressively encloses a larger fraction of the airfoil surfaces and points towards the direction of the local viscous flow streamlines (+s direction). The latter statement follows from the sign of the dominant defect balance component $\mathcal{M}$ being strictly positive, i.e $\boldsymbol{\mathcal{M}} \cdot \hat{s} = \iint (V_e - V)\rho V \, d\mathcal{S} > 0$. Notice that if the fluid viscosity is exactly zero, the boundary layer thickness goes to zero and the RVF and EIF coincide such that the nearfield defect force definition (14) goes to zero. Similarly, the three farfield terms (15) - (17) vanish because $\mathcal{S}_{\text{TP}} \rightarrow 0, \tau = 0$ and the expected D'Alembert paradox is recovered.

The convention of the geometric pressure and suction side definitions used in this discussion retain a degree of physical arbitrariness because the "aerodynamic" split between the upper and lower surface fluid flow streams is determined by the upstream stagnation point[‡]. The latter does not necessarily coincide with the geometric leading edge and its location varies with body shape (symmetric or not) and AoA under consideration. The implication is that a physically accurate breakdown of the defect force into suction $\mathcal{F}_{suction}$ and pressure $\mathcal{F}_{pressure}$ side components is dictated by the stagnation point. In adopting the conventional geometric split of the airfoil surfaces, one should consider that a part of the defect force vector acting on the geometric pressure side in close proximity of the leading edge (see highlighted red region) may yield locally $\mathcal{F}(s) < 0$ contributions for $a > 0$ and vice versa. Hereafter, the geometric convention is adopted for numerical convenience by noting that any negative contributions in close proximity of the trailing edge are merely a matter of "accounting" convention. Resolution of $\mathcal{F}$ about the airfoil's principal axes yields a natural decomposition of the defect force into its drag $\mathcal{F}_D = \mathcal{F}_{D,suction} + \mathcal{F}_{D,pressure}$, and lift $\mathcal{F}_{\mathcal{L}} = \mathcal{F}_{\mathcal{L},suction} + \mathcal{F}_{\mathcal{L},pressure}$ components at a given position s. The defect lift component is exactly zero for non-lifting flows[§] such that the defect force is a measure of the defect drag generation along the flow path. Conversely, the defect lift component of lifting flows is the resultant of partial self-cancellation between the aerodynamic suction and pressure side. For the purposes of the present paper, the analysis will focus on on the defect drag component.

Along the wake, the s-direction follows the trailing edge streamline which divides the upper and lower shear layer flows. At some distance downstream of the trailing edge, the flow aligns with the $\mathbf{V}_\infty$ direction, thereby yielding a pure drag component. At this instance, the defect force generation process terminates with the defect force attaining its final value $\mathcal{F}_\infty$ which equals to the conventional profile drag. This is evident by considering a farther downstream wake position where the pressure field of the airfoil subsides and the semi-expanded wake flow transitions to a fully-expanded free shear layer. The $\mathcal{P}$ dependence is subsequently dropped and the defect force is obtained in the form of the streamwise

[‡]For a 3D flow, the stagnation locus needs to be identified along the width of the fore body.

[§]The magnitude of the defect force from the upper and lower sides is equal and its direction symmetric about the chord line such that the drag and lift-component add up and cancel out at each position, respectively.

momentum defect pertubation within the wake:

$$\mathcal{F}_\infty = \boldsymbol{\mathcal{M}}_\infty \cdot \hat{s} = \iint (V_\infty - V)\rho V \, d\mathcal{S}_{\mathrm{TP}} \tag{18}$$

where the right-hand side equality has been reduced to the conventional far-downstream wake momentum defect relation, as obtained from integral boundary layer relations [31] or farfield methods [3–5].

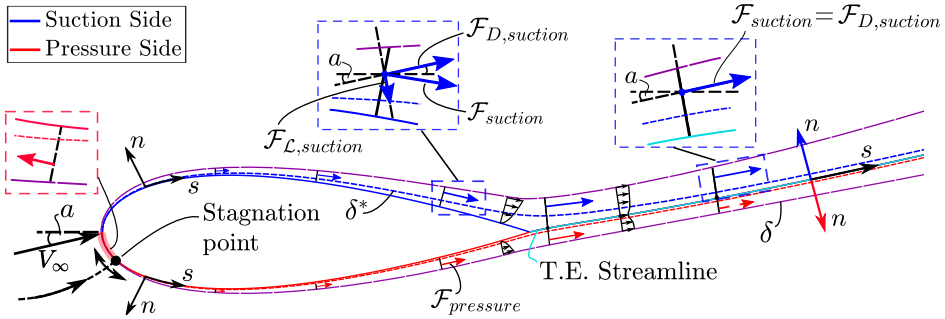


Fig. 3 Defect force definitions over an airfoil and the wake.

C. Defect Force Decomposition Examples

The evolution of the defect force components of Eq. (13), normalised by the nearfield drag, are plotted in Fig. 4 for a NACA0012 airfoil at fixed $Re_c = 1 \times 10^6$, $M_\infty = 0.3$ and 6 angle of attacks. The effect of AoA on the defect force terms of the suction (blue) and pressure (red) sides is summarized in Fig. 4 a) - c). For a 2D flow field, the stream-wise evolution of $\mathcal{M}(s)$ is a function of the momentum thickness, i.e $\mathcal{M}(s) = \rho_e V_e^2 \theta$ thereby growing monotonically along the airfoil surfaces. For $a = 0$, the flow field and thereby the generated defect force vector field is symmetric about the chord line of the airfoil with the suction and pressure side contributions being superimposed[¶]. Conversely, higher a values shift larger fractions of the generated momentum defect towards the suction side by deflecting the upstream stagnation streamline and the corresponding stagnation point towards the pressure side. This favours the earlier growth of the upper boundary layer (initiates at the pressure side now) and the formation of a near-leading edge shear layer zone of higher and subtler acceleration along the suction and pressure side directions, respectively. The extension and severity of the near-leading edge "overspeed" region increases for higher a values and manifests on the upper surface as a steeper increase in the streamwise momentum defect generation rate, $d\mathcal{M}/ds$. Finally, a notable increase in $d\mathcal{M}/ds$ is observed along the airfoil's adverse pressure gradient aft section which is primarily driven by the sharp momentum thickness growth rate $d\theta/ds$ dominating over the local $\rho_e V_e^2$ reduction. Along the wake, the viscous flow gradually transitions to free-stream conditions and the momentum defect gradually asymptotes to its final value $\mathcal{M}_\infty = \mathcal{F}_\infty$ measuring all the

[¶]A notable numerical deviation is present along the wake due to slight miscalculation of the streamline boundary that splits the upper and lower surface contributions. This results in momentum deficient zones being wrongly accounted to the opposite surface, but does not affect the total contribution from both surfaces.

upstream profile drag.

Whereas $\mathcal{M}$ is a useful conceptual means of understanding and quantifying drag (via the M_∞ definition), its physical interpretation is, to a degree, ambiguous. This is because its total (suction+pressure side) peak value exceeds the total nearfield drag close to the trailing edge (see Fig. 4 d) for reference), so that its streamwise evolution does not allow for an explicit causal relation to drag generation. Instead, the pressure defect definition (16), shown in Fig. 4 b), must be incorporated in the analysis. In contrast with the $\mathcal{M}$ term which is strictly positive, the sign of $\mathcal{P}$ varies along the flow path yielding positive and negative contributions spanning accelerative ($p_{G_e} < 0$) and decelerative zones ($p_{G_e} > 0$), respectively. This is evident qualitatively by dropping the first right-hand side term in Eq. (16) assuming pressure invariance across the boundary layer, such that $\partial p/\partial n \approx 0$. Thus, the defect pressure evolution is governed by the product of the gauge edge pressure and the viscous displacement, i.e $\mathcal{P} \approx p_{G_e}\delta^*$. Noting that δ^* is strictly positive and grows monotonically along the airfoil surfaces, it follows that the local magnitude of $\mathcal{P}$ is maximum along regions of high flow acceleration/deceleration acting on zones of large viscous displacement. Thus, the position of the peak $\mathcal{P}$ value is determined by the "optimum" trade-off between moderate favourable pressure gradients and sufficient viscous displacement growth and remains nearly constant with angle of attack (at $x/c \approx 0.4$) for the scenarios tested. On the other hand, the minimum $\mathcal{P}$ value is expected to occur in the near vicinity of the trailing edge, since the presence of strong adverse pressure gradients favours the rapid growth of δ^* which attains its maximum value at the trailing edge. With reference to the superpositioned $\mathcal{P}$ curves of $a = 0°$, higher angles of attack act as an amplifier and damper for the suction and pressure sides, respectively via their effect on the stagnation point location (see discussion above) without affecting the monotonicity of the curves and the position of the minimum and maximum $\mathcal{P}$ values. Downstream of the trailing edge, the pressure field of the body rapidly subsides and the affiliated pressure defect component asymptotes to zero, as expected.

The resultant defect force evolution of the suction and pressure sides is thus measured by the sum of $\mathcal{M} + \mathcal{P}$ [‖], as shown in Fig. 4 c). The $\mathcal{F}$ curves closely resemble the respective dominant momentum defect component with the local $\mathcal{P}$ contributions acting towards magnifying the local streamwise growth rate $d(\mathcal{M} + \mathcal{P})/ds$ of the defect force along accelerative regions and towards balancing out the large $\mathcal{M}$ contributions along the near trailing edge region. The deviation of the defect force from $\mathcal{M}$ is largely driven by a, with higher values of the latter yielding more notable effects along the suction side and a subsequent monotonicity change upstream of the trailing edge. Contrarily, higher a values progressively suppress pressure field pertubations along the pressure side, with the resulting defect force evolution remaining relative insensitive to $\mathcal{P}$ (for the reasons explained before) and well approximated as $\mathcal{F}_{pressure} \approx \mathcal{M}$ for the highest a regime tested. The total defect force evolution, shown in Fig. 4 d), follows from the sum of the suction and pressure side contributions and accumulates monotonically along the airfoil and the near wake region ($x/c \approx 1.5c$), whereafter it asymptotes to the total viscous drag. This "lag" between the nearfield drag and its farfield

[‖] The $\mathcal{T}$ component is dropped from the analysis as being negligible relative to the others.

defect manifestation lies in the defect flow force definition which is derived with reference to the EIF rather than the simple inviscid flow, with the former being associated with an effective body which extends to the wake region. Thus, the position where the notions of the "defect drag" (defect component parallel to $\mathbf{V}_\infty$) and drag coincide is subject to the shape and wake extent of the EIB, both varying with operating conditions, a and the bluntness of the real aerodynamic body. For the conditions tested, the EIB curvature rapidly subsides and the EIB "walls" align (approximately) with the free-stream flow direction, yielding drag estimates within $\sim 1-3\%$ of the nearfield drag without any apparent loss of accuracy for higher AoA.

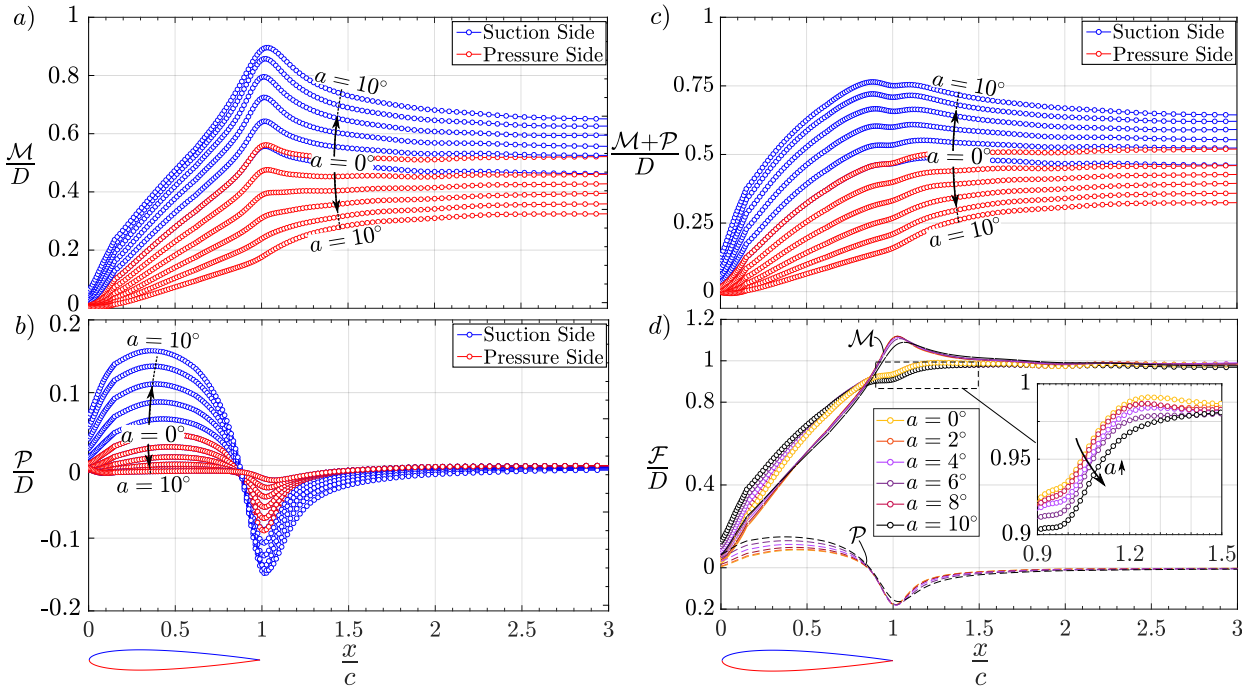


Fig. 4 Drag-normalised defect force component evolutions for NACA0012 airfoil at $Re_c = 1 \times 10^6$, $M_\infty = 0.3$ and $\alpha = 0, 2, 4, 6, 8, 10$: a) - c) Individual evolutions from suction and pressure sides. d) Total (pressure + suction side) defect force components.

1. Defect Drag Generation

The notional breakdown of the aerodynamic defect force along the principal aerodynamic axes offers a physical means of defining and tracing the streamwise "defect drag" ($\mathcal{F}_\mathcal{D}$) generation and its subsequent manifestation as profile drag in the wake, as shown in Fig. 5 for three AoA. For this relatively thin airfoil, the respective $\mathcal{F}$ evolutions are closely matching their respective $\mathcal{F}_D$ curves along the flow path except for the near trailing edge region, where the misalignment between the $\mathbf{V}_\infty$ direction and the local curvature is more pronounced. The upward shift of the $\mathcal{F}, \mathcal{F}_D$ curves with increasing a in the near leading edge region signifies that the affiliated "overspeed" penalty along the suction side results in excess defect drag generation. Note that $\mathcal{F}_D$ measures the sum of the conventional nearfield friction drag and the pressure defect drag component, with the former terminating at the trailing edge such that the residual wake defect

drag explicitly captures a portion of the pressure defect drag associated with the wake-extent of the EIB. In the authors' opinion, the notion of the defect drag more closely resembles the physical principles of (viscous) drag, because the defect force accounts for the "force pertubation" of the RVF with respect to the "viscosity-corrected" potential flow field and thereby, it can be meaningfully traced along partial wall surfaces. This means that the defect drag definition enables the calculation of drag contributions when only a part of the aerodynamic body is modelled in CFD. Another potential advantage is that the numerical and experimental implementation of the defect force balance (13) for the extraction of the viscous drag only requires high resolution measurements of readily available flow field data across a free-shear layer plane that is positioned in close proximity from the trailing edge.

For completeness, the lift (per unit span) component $\mathcal{F}_\mathcal{L}$ is additionally superimposed in the graph. This appears to be strictly negative, indicating that viscous effects are affiliated with a loss of local lift production, which monotonically grows along the airframe surfaces, thereby attaining its maximum magnitude at the trailing edge. The slope $d\mathcal{F}_\mathcal{L}/dx$ is controlled by the angle of attack, with higher AoA values leading to more notable loss magnitudes. A more detailed discussion about the implication of this component is out of scope for the present research and a better understanding of its physical implications is required in the future. It is unclear to the authors whether that local loss of lift described by $\mathcal{F}_\mathcal{L}$ is closely affiliated with the viscous decambering mechanism described by Drela [27] or if it corresponds to an additional penalty.

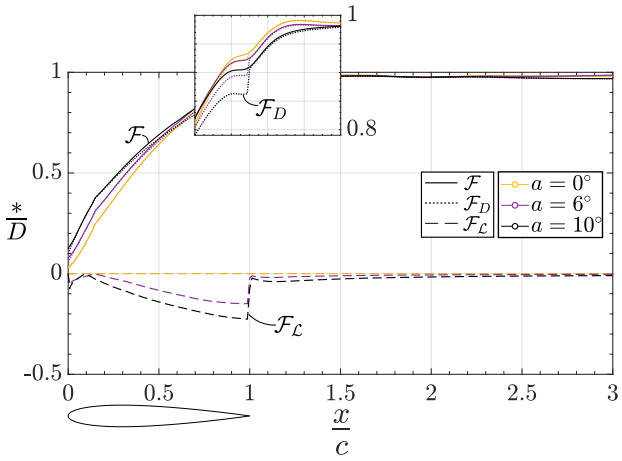


Fig. 5 Drag-normalised defect force, defect drag and defect lift component evolutions for a NACA0012 airfoil at $Re_c = 1 \times 10^6$, $M_\infty = 0.3$ and $\alpha = 0, 6, 10$.

2. Effects of Operating Conditions and Wall Temperature

The evolution of the momentum defect components of a NACA0012 airfoil at fixed $a = 4°$ and for various operating conditions, expressed non-dimensionally as a function of Re_c, M_∞ and T_w/T_∞, is shown in Fig. 6 a) - c). The overall characteristics of the individual $\mathcal{M}, \mathcal{P}$ and total defect force components remain invariant to changes in the examined parameters. As shown in Fig. 6 a), increasing Re_c has a marginal effect on the defect force evolution with the dominant

$\mathcal{M}$ and $\mathcal{P}$ component curves being almost superimposed, despite the apparent Re_c dependency of the viscous flow characteristics (boundary layer shape profile). That is, the spatial distribution of the defect force generation process is largely insensitive to the boundary layer profile and the weak Re_c dependence of $\mathcal{F}$ is implicitly imposed via the effect of Reynolds number on the viscous displacement (and thus $\mathcal{P}$, as shown in Fig. 6 d)).

In the absence of shockwaves, the defect force evolution also appears to be nearly invariant to M_∞ changes, as shown in Fig. 6 b), despite the non-negligible variation among its components. This is mainly due to the opposing dependence of $\mathcal{M}$ and $\mathcal{P}$ on M_∞ which yields a quasi "self-cancellation" net effect. Higher M_∞ flows give rise to "compressible thickening" of the EIB (see Fig. 6 d)) due to density variations inside the shear layer which increase the magnitude of $\mathcal{P}$ along regions of strong pressure gradient. Conversely, the corresponding streamwise momentum defect growth $d\mathcal{M}/ds$ varies weakly due to density pertubations that partially suppress the $\rho_e V_e^2$ factor (and thus $\mathcal{M}$) when $dV_e/ds > 0$ and slightly increase θ for $dV_e/ds < 0$.

The effect of varying the wall temperature T_w/T_∞ is shown in Fig. 6 c), for adiabatic, uniformly cooled and heated airfoil walls. The presence of strong heat transfer effects leads to the development of a thermal boundary layer field "independently" from the viscous boundary layer favouring notable thermally-induced density variations across the thermal boundary layer, regardless of the free-stream compressibility. Relative to the adiabatic reference flow, wall cooling yields a density excess $\rho/\rho_{\text{ad}} > 0$ inside the boundary layer thereby reducing δ^* [39] and favouring the formation of a thinner effective body (see Fig. 6 d)) and vice versa. Alongside the effects on density, varying T_w/T_∞ alters the dissipative characteristics of the boundary layer, with higher T_w/T_∞ reducing the "effective Reynolds number" of the flow [40]. However, Fig. 6 a) and b) signify that the evolution of the defect components is nearly Re_c independent so that local $\mathcal{M}$ and $\mathcal{P}$ variations are primarily triggered by thermo-compressible interference effects either due to free-stream compressibility and curvature or due to the presence of heat sources (or sinks) in the flow field.

IV. Defect Mechanical Energy Equation

A. Formulation

In the absence of body forces, the RRF steady-state Reynolds-averaged mechanical energy equation in divergence form is obtained from the dot product of the momentum equation (9) with the local velocity vector, $\boldsymbol{V}$ [17]:

$$\frac{1}{2}\nabla \cdot (\rho \boldsymbol{V} V^2) = -(\nabla p \cdot \boldsymbol{V}) + (\nabla \cdot \bar{\bar{\tau}}) \cdot \boldsymbol{V} \tag{19}$$

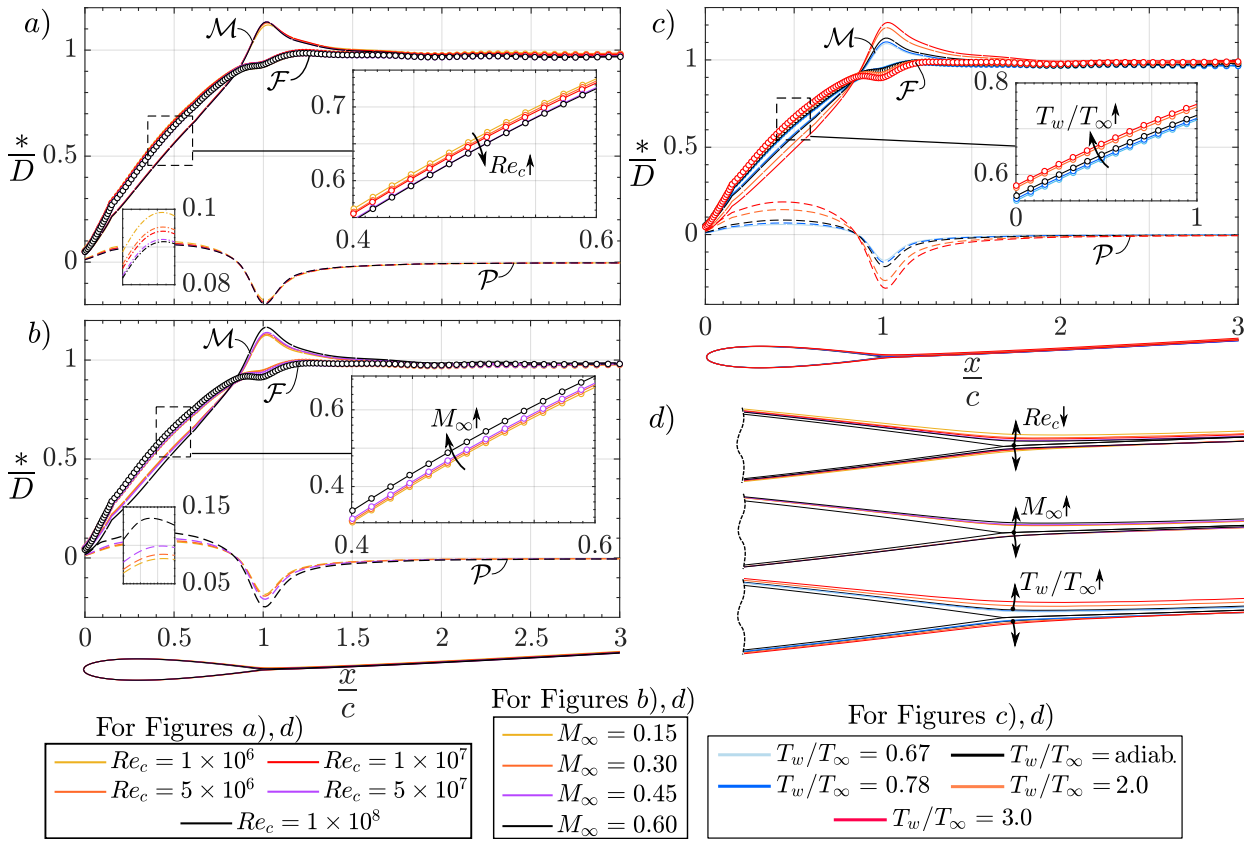


Fig. 6 Drag-normalised (suction + pressure side) defect force component evolutions for NACA0012 airfoil at constant $a = 4°$ and various operating conditions.

The defect mechanical energy equation in differential form is obtained by subtracting the EIF from the RVF mechanical energy equation:

$$\begin{aligned}\frac{1}{2}\nabla\cdot(\rho_e \boldsymbol{V}_e V_e^2 - \rho \boldsymbol{V} V^2) &= -(\nabla p_e \cdot \boldsymbol{V}_e - \nabla p \cdot \boldsymbol{V}) - (\nabla\cdot\bar{\bar{\tau}})\cdot\boldsymbol{V} \\ &= -\nabla\cdot(p_e\boldsymbol{V}_e - p\boldsymbol{V}) - \nabla\cdot(\bar{\bar{\tau}}\cdot\boldsymbol{V}) + p_e\nabla\cdot\boldsymbol{V}_e - p\nabla\cdot\boldsymbol{V} + (\bar{\bar{\tau}}\cdot\nabla)\cdot\boldsymbol{V}\end{aligned} \tag{20}$$

where the right-hand side expansion follows from the vector identities:

$$\nabla\cdot(p\boldsymbol{V}) = \nabla p\cdot\boldsymbol{V} + p\nabla\cdot\boldsymbol{V} \tag{21}$$

$$\nabla\cdot(\bar{\bar{\tau}}\cdot\boldsymbol{V}) = (\nabla\cdot\bar{\bar{\tau}})\cdot\boldsymbol{V} + (\bar{\bar{\tau}}\cdot\nabla)\cdot\boldsymbol{V} \tag{22}$$

Volume integration of (20) and use of the Gauss identities (4), (5) yields:

$$\oiint \frac{1}{2}\rho_e \boldsymbol{V}_e V_e^2 \cdot \hat{\boldsymbol{n}}\, d\mathcal{S}^* - \oiint \frac{1}{2}\rho \boldsymbol{V} V^2 \cdot \hat{\boldsymbol{n}}\, d\mathcal{S} = -\oiint p_e \boldsymbol{V}_e \cdot \hat{\boldsymbol{n}}\, d\mathcal{S}^* + \oiint p\boldsymbol{V} \cdot \hat{\boldsymbol{n}}\, d\mathcal{S} + \iiint p_e \nabla \cdot \boldsymbol{V}_e\, d\mathcal{V}^* - \iiint p \nabla \cdot \boldsymbol{V}\, d\mathcal{V} + \iiint (\bar{\bar{\tau}} \cdot \nabla) \cdot \boldsymbol{V}\, d\mathcal{V} + \oiint -(\bar{\bar{\tau}} \cdot \boldsymbol{V}) \cdot \hat{\boldsymbol{n}}\, d\mathcal{S} \quad (23)$$

Expansion of the kinetic energy rate term along with the continuity equation (8) yields a simplification of the LHS in the form of a single Trefftz plane kinetic defect integral:

$$\oiint \frac{1}{2} V_e^2 \rho_e \boldsymbol{V}_e \cdot \hat{\boldsymbol{n}}\, d\mathcal{S}^* - \oiint \frac{1}{2} V^2 \rho \boldsymbol{V} \cdot \hat{\boldsymbol{n}}\, d\mathcal{S} = \iint (\frac{1}{2} V_e^2 \rho_e \boldsymbol{V}_e - \frac{1}{2} V^2 \rho \boldsymbol{V}) \cdot \hat{\boldsymbol{n}}\, d\mathcal{S}_{\mathrm{TP}} - \iint \frac{1}{2} V_e^2 \rho_e \boldsymbol{V}_e \cdot \hat{\boldsymbol{n}}\, d\mathcal{S}_{\mathrm{TP}}^{\delta^*} = \iint [\frac{1}{2}(V_e^2 - V^2)\rho \boldsymbol{V})] \cdot \hat{\boldsymbol{n}}\, d\mathcal{S}_{\mathrm{TP}} + \underbrace{\frac{1}{2} V_e^2 \left(\iint (\rho_e \boldsymbol{V}_e - \rho \boldsymbol{V}) \cdot \hat{\boldsymbol{n}}\, d\mathcal{S}_{\mathrm{TP}} - \iint \rho_e \boldsymbol{V}_e \cdot \hat{\boldsymbol{n}}\, d\mathcal{S}_{\mathrm{TP}}^{\delta^*} \right)}_{=0} = \iint \frac{V_e^2 - V^2}{2} \rho \boldsymbol{V} \cdot \hat{\boldsymbol{n}}\, d\mathcal{S}_{\mathrm{TP}} \quad (24)$$

Substitution of (24) into (23) yields the final form of the integral mechanical energy defect equation:

$$\iint \left(\frac{V_e^2 - V^2}{2} \right) \rho \boldsymbol{V} \cdot \hat{\boldsymbol{n}}\, d\mathcal{S}_{\mathrm{TP}} + \oiint p_{G_e} \boldsymbol{V}_e \cdot \hat{\boldsymbol{n}}\, d\mathcal{S}^* - \oiint p_G \boldsymbol{V} \cdot \hat{\boldsymbol{n}}\, d\mathcal{S} = \iiint (p_{G_e} \nabla \cdot \boldsymbol{V}_e - p_G \nabla \cdot \boldsymbol{V})\, d\mathcal{V} - \iiint p_{G_e} \nabla \cdot \boldsymbol{V}_e\, d\mathcal{V}_{\delta^*} + \iiint (\bar{\bar{\tau}} \cdot \nabla) \cdot \boldsymbol{V}\, d\mathcal{V} + \oiint -(\bar{\bar{\tau}} \cdot \boldsymbol{V}) \cdot \hat{\boldsymbol{n}}\, d\mathcal{S} \quad (25)$$

where the substitution of the gauge pressure $p_G \rightarrow p - p_\infty$ is permissible from the Gauss identities:

$$\oiint p_\infty \boldsymbol{V} \cdot \hat{\boldsymbol{n}}\, d\mathcal{S} = p_\infty \iiint \nabla \cdot \boldsymbol{V} \text{ and } \oiint p_\infty \boldsymbol{V}_e \cdot \hat{\boldsymbol{n}}\, d\mathcal{S} = p_\infty \iiint \nabla \cdot \boldsymbol{V}_e\, d\mathcal{V} \quad (26)$$

Equation (25) yields the final RRF defect mechanical energy balance, that governs the mechanical loss generation inside the flow field:

$$\underbrace{\Phi + \mathcal{B}}_{\Phi^*} = \dot{\mathcal{E}}_{\mathcal{K}} + \dot{\mathcal{E}}_{\mathcal{P}} + \dot{\mathcal{E}}_{\tau} \quad (27)$$

The left hand-side terms of Eq. (27) account for the accumulated volumetric mechanical loss generation (Φ^*), while the right-hand side energy flux rates, their defect-flux manifestation. The terms are defined hereafter:
Viscous dissipation rate Φ [17],

$$\Phi = \iiint (\bar{\bar{\tau}} \cdot \nabla) \cdot \boldsymbol{V}\, d\mathcal{V} \quad (28)$$

This is the viscous loss mechanism that converts the kinetic energy of the shear layer flow into volumetric heat due to fluid deformation. It manifests inside viscous regions such as boundary layers, free shear layers and shock waves and is the driving profile loss generation mechanism for subsonic and transonic flows.

Baroclinic power $\mathcal{B}$,

$$\mathcal{B} = \iiint (p_{G_e} \nabla \cdot \boldsymbol{V}_e - p_G \nabla \cdot \boldsymbol{V})\, d\mathcal{V} - \iiint p_{G_e} \nabla \cdot \boldsymbol{V}_e\, d\mathcal{V}_{\delta^*} \tag{29}$$

This is the volumetric compressibility-induced power imparted to the flow due to non isentropic expansion and compression. This term contains non-negligible loss contributions when heat is deposited into compressive and expansive flow regions and acts as a power source when strong heat absorption/cooling effects are present. For subsonic adiabatic flows, the underlying loss mechanism is the viscous self-heating of shear layers acting on highly compressible regions (near leading and trailing edge regions). For incompressible flows, Eq. (29) becomes zero due to the dilation term relation $\nabla \cdot \boldsymbol{V} = -\mathrm{D}(ln\rho)/\mathrm{D}t = 0$.

The kinetic energy defect rate $\dot{\mathcal{E}}_{\mathcal{K}}$,

$$\dot{\mathcal{E}}_{\mathcal{K}} = \iint \left(\frac{V_e^2 - V^2}{2} \right) \rho \boldsymbol{V} \cdot \hat{\boldsymbol{n}}\, d\mathcal{S}_{\mathrm{TP}} \tag{30}$$

This is the kinetic energy defect outflow rate convected by the shear layer across the Trefftz plane. For a 2D flow field, this term reduces to the conventional kinetic energy defect $\frac{1}{2}\rho_e V_e^3 \theta^*$ and appears in the dimensional integral kinetic energy equation [31]. It measures approximately the total upstream dissipation losses for incompressible flow [17] and subsonic flows without strong heat transfer effects.

The pressure-work defect rate $\dot{\mathcal{E}}_{\mathcal{P}}$,

$$\dot{\mathcal{E}}_{\mathcal{P}} = \iint (p_{G_e} \boldsymbol{V}_e - p_G \boldsymbol{V}) \cdot \hat{\boldsymbol{n}}\, d\mathcal{S}_{\mathrm{TP}} - \iint p_{G_e} \boldsymbol{V}_e \cdot \hat{\boldsymbol{n}}\, d\mathcal{S}_{\mathrm{TP}}^{\delta^*} \tag{31}$$

This is the rate of defect pressure work done on the boundary layer transversing the Trefftz plane. It contains positive contributions along regions of favourable pressure gradients and substantial negative contributions along regions with flow deceleration and large viscous displacement.

The viscous boundary work rate $\dot{\mathcal{E}}_{\tau}$,

$$\dot{\mathcal{E}}_{\tau} = \iint (\bar{\bar{\tau}} \cdot \boldsymbol{V}) \cdot \hat{\boldsymbol{n}}\, d\mathcal{S}_{\mathrm{TP}} \tag{32}$$

this is the rate of shear stress work done on the boundary layer flow transversing the Trefftz plane and is present in the conventional RVF mechanical energy equation (see for example Ref. [18]). This term yields larger positive contributions for accelerative boundary layers and becomes rapidly negligible along the wake due to the dissipative decay of velocity

pertubations.

B. Mechanical Loss Characterisation and Estimation

1. Shear Layer Dissipation

In the absence of shock waves, the total dissipation, Φ_∞, imparted to the flow for a Trefftz plane positioned at an infinite distance downstream the aerodynamic body, is measured as the sum of the individual contributions from the boundary layer dissipation, Φ_{BL} and the wake dissipation, Φ_{wake}:

$$\Phi_\infty = \Phi_{\text{BL}} + \Phi_{\text{wake}} \tag{33}$$

Φ is a positive scalar quantity so that its notional breakdown in Eq. (33) is physically justified. The evolution of the local dissipative shear layer characteristics is more conveniently expressed in terms of the dissipation coefficient ($C_\mathcal{D}$), which for a 2D shear layer, yields:

$$C_\mathcal{D} = \frac{\mathcal{D}}{\rho_e V_e^3} \tag{34}$$

where the enumerator in Eq. (34) is the dissipation rate $\mathcal{D}$ across the shear layer, given by Eq. (C8). Substitution of the $C_\mathcal{D}$ definition (34) into the dissipation relation (33), yields a unique relation between the rate of change of viscous dissipation $d\Phi/ds$ as a function of local shear layer properties:

$$\Phi_\infty = \int_{\text{BL}} \rho_e V_e^3 C_\mathcal{D}\, ds + \int_{\text{wake}} \rho_e V_e^3 C_\mathcal{D}\, ds \tag{35}$$

In Eq. (34), the magnitude of $C_\mathcal{D}$ is relatively insensitive to pressure gradients [17, 26, 31], meaning that dissipative losses are primarily governed by the $\sim V_e^3$ scaling and less from changes in $C_\mathcal{D}$ magnitude. Conversely, the dissipative characteristics of the wake are primarily driven by the steep decrease in the rate of change of $dC_\mathcal{D}/ds$ along the flow path due to the viscous attenuation of the free shear layer flow at nearly constant $\rho_e V_e^3 \approx \rho_\infty V_\infty^3$. The latter statement is invalid downstream of the trailing edge, where a transitional semi-expanded region is formed in response to the pressure field of the aerodynamic body. The transitional region terminates approximately when the wake portion of the effective body's camber shape restores its symmetry about the streamwise direction, as indicated in Fig. 7. For a fully or quasi-fully expanded flow, the baroclinic power contributions also go to zero, such that its generation is primarily confined along the upstream airframe surfaces.

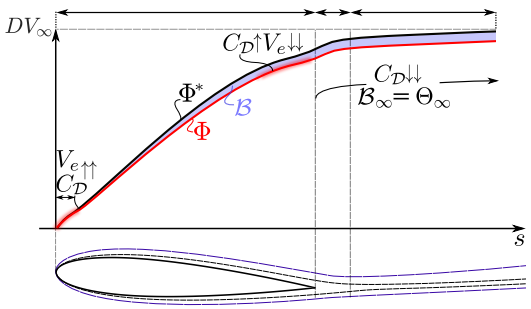


Fig. 7 Mechanical energy loss (Φ^*) and viscous dissipation (Φ) evolution for adiabatic compressible viscous flow. The deviation between the two trends is attributed to the additional baroclinic power imparted to the flow.

2. Baroclinic Power

Following the notation by Sanders and Laskaridis [18], the volumetric pressure power Θ imparted to the real viscous flow is obtained as:

$$\Theta = -\iiint p_G \nabla \cdot \boldsymbol{V}\, d\mathcal{V} \tag{36}$$

This term accounts for the RVF thermo-compressible energy exchange (via the dilatation term $\nabla \cdot \boldsymbol{V}$) spanning over regions of strong pressure gradients, such as stagnation point regions and body surfaces with substantial curvature variations, favouring flow acceleration ($\Theta < 0$) and deceleration ($\Theta > 0$). In contrast with Φ, local Θ contributions do not represent losses, instead those measure the sum of the upstream isentropic and baroclinic contributions at each point, yielding the following notional Θ decomposition:

$$\Theta = \Theta_r + \mathcal{B} \tag{37}$$

where Θ_r accounts for isentropic thermo-compressible energy transfer due to compression and expansion of the outer potential flow field that naturally self-recovers, resulting in zero farfield power deposition for a fully expanded flow. The latter statement follows directly from the Gibbs equation over an isentropic streamtube with its mass flux boundaries lying in the free-stream, as detailed in Appendix D. Conversely, the baroclinic power definition (29) represents the entropic thermo-compressible power trace associated with the alteration of the local compressibility characteristics of shear layers relative to EIF due to heat transfer effects. This term behaves as a power sink ($\mathcal{B} > 0$) and power source ($\mathcal{B} < 0$) for heat deposition and absorption, respectively.

For typical adiabatic subsonic flows, $\mathcal{B} > 0$ with the driving heat deposition mechanism being the self-heating of shear layers via viscous dissipation, leading to a mechanical loss excess $\Phi^* > \Phi$, as shown qualitatively in Fig. 7. For transonic flows, the formation of shock waves lead to additional baroclinic losses ($\mathcal{B}_{\text{shock}}$) which may be approximately incorporated within the defect analysis via the approximate procedure described in Appendix E. However, a more detailed discussion of shock-related implications will not be addressed in the present work. For the general non-adiabatic

wall scenario, heated and cooled walls result in the formation of an "independent" thermal boundary layer field associated with entropy generation $\mathcal{B} > 0$ and entropy reduction $\mathcal{B} < 0$.

The dependence of Θ_r and $\mathcal{B}$ on the gauge pressure indicates that the thermo-compressible energy exchange runs to completion when the viscous flow transitions to a fully-expanded free-shear layer. Therefore, the net baroclinic power trace imparted to the flow asymptotes to the RVF definition of Θ when the latter is integrated over a fully-expanded streamtube enclosing the body:

$$\Theta_\infty = \underbrace{\Theta_{r_\infty}}_{=0} + \mathcal{B}_\infty = \mathcal{B}_\infty \tag{38}$$

where the subsript ∞ denotes a Trefftz plane positioned at a wake position with fully expanded conditions. The right-hand side equality of Eq. (38) follows from the exact self-cancellation of the equivalent isentropic field thereby allowing Θ_∞ to capture the net baroclinic residual. Numerical implications of Eq. (38) as well as the relation between the definition of $\mathcal{B}$ and the baroclinic power definition of Sato [26] will be addressed in subsequent subsections.

3. Total Mechanical Energy Loss Estimation

The calculation of the mechanical energy losses, $\Phi^* = \Phi + \mathcal{B}$, involves the post-processing of Eqs. (28) and (29) that may not be straightforward to estimate from the available flow field data. The right-hand side of Eq. (27) provides a numerically advantageous alternative of estimating Φ^* by means of Trefftz plane measurements. From a wind tunnel perspective, the surface integral representation of Φ^* offers a viable solution of carrying out an energy-based aerodynamic analysis from limited experimental measurements.

Noting that the rear extent of an aerodynamic body's pressure field and thus the semi-expanded wake region, typically decay within a fraction of a chord, the upstream mechanical loss accumulation at any wake position s may be accurately approximated by the free-stream kinetic energy defect, $\dot{\mathcal{E}}_{\mathcal{K}_\infty}$ crossing the Trefftz plane:

$$\Phi^*(s) = \Phi^*_{\text{BL}} + \Phi^*_{\text{wake}}(s) \approx \dot{\mathcal{E}}_{\mathcal{K}_\infty}(s) = \iint \left(\frac{V_\infty^2 - V^2}{2}\right) \rho \boldsymbol{V} \cdot \hat{\boldsymbol{n}}\, d\mathcal{S}_{\text{TP}} \tag{39}$$

The downstream dissipation may be implicitly obtained via wake plane measurements by noting that, from a power balance perspective [17], the integration of the total mechanical energy losses over a CV extending at infinite distance downstream asymptotes to the total drag power of the aerodynamic body, as follows:

$$\Phi^*_\infty = \Phi_\infty + \Theta_\infty \approx DV_\infty \tag{40}$$

Assuming fully-expanded wake flow, the aerodynamic defect force vector aligns with $\mathbf{V}_\infty$, thereby yielding a farfield

profile drag approximation as a function of the free-stream momentum defect outflow magnitude, $\mathcal{M}_\infty$:

$$\mathcal{M}_\infty = \iint (V_\infty - V)\rho V \, d\mathcal{S}_{\text{TP}} \approx D \tag{41}$$

Therefore, the residual wake losses $\Phi^*_{\text{res}}(s) \approx \Phi_{\text{res}}(s)$ at any point downstream of the Trefftz plane are measured by subtracting the upstream mechanical losses $\dot{\mathcal{E}}_{\mathcal{K}_\infty}(s)$ from the total drag power $DV_\infty \approx \dot{\mathcal{E}}_{\mathcal{K}_\infty}(s)$:

$$\Phi^*_{\text{res}} \approx \Phi_{\text{res}} \approx \mathcal{M}_\infty V_\infty - \dot{\mathcal{E}}_{\mathcal{K}_\infty}(s) = \iint \frac{(V - V_\infty)^2}{2} \rho V \, d\mathcal{S}_{\text{TP}} \tag{42}$$

where Eq. (42) coincides with the E_a term of the power balance [17] and states that the kinetic energy excess of the defect shear layer flow measures all the downstream dissipation. By definition, $\mathcal{M}_\infty$ is invariant along the fully expanded wake domain, and thereby independent of the Trefftz plane position. Thus, the momentum defect may be measured at any wake location that is considered numerically or experimentally advantageous. Notice that for a 2D flow, Eq. (42) is directly lift the excess kinetic energy thickness κ definition (C5) as $\Phi^*_{\text{res}} \approx \frac{1}{2}\rho_e V_e^3 \kappa$ for fully-expanded flow.

C. Sato's Defect Mechanical Energy Balance

A more elegant form of the defect mechanical energy equation may be obtained from the following semi-expanded form, assuming the validity of the thin shear layer approximations [26]:

$$\frac{1}{2}\nabla \cdot (\rho_e \boldsymbol{V}_e V_e^2 - \rho \boldsymbol{V} V^2) = -\rho_e \bar{\nabla}\frac{1}{2}V_e^2 \cdot (\boldsymbol{V}_e - \boldsymbol{V}) - \nabla \cdot (\bar{\bar{\tau}} \cdot \boldsymbol{V}) + (\bar{\bar{\tau}} \cdot \nabla) \cdot \boldsymbol{V} \tag{43}$$

where the vector identity (22) has been invoked for the expansion of the viscous term along with the thin shear layer approximation for the edge pressure gradient [26]:

$$\nabla p \simeq \nabla p_e \simeq \bar{\nabla} p_e \simeq \rho_e \bar{\nabla}\frac{1}{2}V_e^2 \tag{44}$$

where $\bar{\nabla} = \partial()/\partial s$, the surface gradient of a 2D flow. For a 3D shear layer, an additional component would be required for the treatment of the gradient in the cross-flow direction. Integration of the mechanical energy relation (43) over the RVF and EIF control volumes and use of the Gauss's identities (4), (5), the defect continuity relation (7) and kinetic defect identity (24) yield Sato's [26] integral defect mechanical energy equation:

$$\Phi - \int \mathbf{D}^{**} \cdot \bar{\nabla}\frac{1}{2}V_e^2 \, ds = \dot{\mathcal{E}}_{\mathcal{K}} + \dot{\mathcal{E}}_\tau \tag{45}$$

where the derivation makes use of the boundary layer defects (C1), (C3), (C7) as well as the following properties:

$$\iiint -\rho_e \bar{\nabla} \frac{1}{2} V_e^2 \cdot \boldsymbol{V}_e \, d\mathcal{V} - \iiint -\rho_e \bar{\nabla} \frac{1}{2} V_e^2 \cdot \boldsymbol{V}_e \, d\mathcal{V}^* = \iiint -\rho_e \bar{\nabla} \frac{1}{2} V_e^2 \cdot (\boldsymbol{V}_e - \boldsymbol{V}) \, d\mathcal{V} - \iiint -\rho_e \bar{\nabla} \frac{1}{2} V_e^2 \cdot \boldsymbol{V}_e \, d\mathcal{V}_{\delta^*} \quad (46)$$

$$\iiint -\rho_e \bar{\nabla} \frac{1}{2} V_e^2 \cdot (\boldsymbol{V}_e - \boldsymbol{V}) \, d\mathcal{V} = \int -\rho_e \bar{\nabla} \frac{1}{2} V_e^2 \cdot \boldsymbol{Q} \, ds \quad (47)$$

$$\iiint -\rho_e \bar{\nabla} \frac{1}{2} V_e^2 \cdot \boldsymbol{V}_e \, d\mathcal{V}_{\delta^*} = \int \bar{\nabla} \frac{1}{2} V_e^2 \iint \rho_e \boldsymbol{V}_e \, d\mathcal{S}_{\mathrm{TP}}^{\delta^*} \, ds = \int \bar{\nabla} \frac{1}{2} V_e^2 \iint [\rho_e \boldsymbol{V}_e - \rho \boldsymbol{V}] \cdot \hat{\boldsymbol{n}} \, d\mathcal{S}_{\mathrm{TP}} \, ds \quad (48)$$

Relative to Sato's derivation [26], Eq. (45) has been derived directly from the conservation form of the generalised defect mechanical energy equation based on the concept of the fictitious body rather than the less intuitive transpiration wall model [27]. The TSL approximations yield now an elegant formulation of compressibility-induced effects that lumps the net $(\mathcal{B} - \mathcal{E}_{\mathcal{P}})$ effect[**] under a single baroclinic power term $-\Pi_V$ that is function of the density flux defect $\mathbf{D}^{**}$ (C3) and the gradient of the squared edge velocity gradient:

$$-\Pi_V = -\int \mathbf{D}^{**} \cdot \bar{\nabla} \frac{1}{2} V_e^2 \, ds \quad (49)$$

1. Baroclinicity-Corrected Dissipation

An elegant way of incorporating $-\Pi_V$ into a single mechanical loss integral Φ^* has been derived by Sato [26] in the form of a baroclinicity-corrected dissipation integral assuming adiabatic flow, a near-unity free-stream Prandtl number $\mathrm{Pr} \simeq 1$ and weak flow acceleration. The resulting mechanical loss approximation is now expressed as a function of the dissipation coefficient $C_{\mathcal{D}}$ and the local edge flow compressibility characteristics:

$$\Phi^* \simeq \frac{\int \rho_e V_e^3 \left(1 + \frac{\gamma - 1}{2} M_e^2\right)^r C_{\mathcal{D}} \, ds}{\left(\frac{\gamma - 1}{2} M_e^2\right)^r \Big|_{\mathrm{TP}}} \quad (50)$$

where γ the specific heat ratio, M_e the edge Mach number and $r \simeq \mathrm{Pr}^{0.5}$ the temperature recovery factor as obtained from a compressible (laminar) flat plate flow [41].

D. Test Cases

The evolution of the mechanical loss components of Eq. (27), normalised by the nearfield drag power DV_∞, are plotted in Fig. 8 for the suction and pressure sides of a NACA0012 airfoil at fixed $Re_c = 1 \times 10^6$, $M_\infty = 0.3$ and 6 angle

[**]This is evident by matching terms between the defect mechanical energy balance (27) and Sato's corresponding formulation (45).

of attacks. For this 2D flow, the kinetic energy defect rate can be expressed as $\dot{\mathcal{E}}_{\mathcal{K}} = \rho_e V_e^3 \theta^*$ which is closely related to viscous dissipation [17] and is therefore a strictly positive quantity. For these subsonic conditions, density variations are relatively small compared to the affiliated V_e^3 factor, indicating that the near leading edge acceleration, which is magnified for higher AoA, is affiliated with a rapid growth of $d\dot{\mathcal{E}}_{\mathcal{K}}/ds$ and therefore, mechanical losses. On the other hand, regions of mild acceleration or strong deceleration along the midbody and the aft portion of the airfoil experience a notable reduction in V_e^3 and therefore $d\dot{\mathcal{E}}_{\mathcal{K}}/ds$. The maximum $\dot{\mathcal{E}}_{\mathcal{K}}$ value is attained close to the trailing edge for the suction side of high AoA flows, with the respective pressure side kinetic defect evolution monotonically increasing along the wake. This counter-intuitive behaviour is analogous to the corresponding $\mathcal{M}$ component of the defect force balance (13), and underlines the physical ambiguity involved in conventional boundary layer formulations [31] or Sato's balance (45). In these formulations, the effect of pressure gradients manifests only as a compressibility by-product via the $\delta^{**} = 0$ term. This approximation follows from the assumption of constant pressure across the boundary layer and implies that $\dot{\mathcal{E}}_{\mathcal{K}} = \Phi$ for incompressible flow. However, this is not strictly true since $d\dot{\mathcal{E}}_{\mathcal{K}}/ds$ obtains both positive and negative values (see the $\dot{\mathcal{E}}_{\mathcal{K}}$ reduction in the suction side wake) whereas the corresponding viscous accumulation rate $d\Phi/ds$ is a strictly positive quantity.

Instead, Eq. (27) indicates that even for subsonic adiabatic viscous flows with $\mathcal{B} \approx 0$, the upstream dissipation generation is measured by the net mechanical energy defect rate across the shear layer $\mathcal{E}_{\mathcal{K}} + \mathcal{E}_{\mathcal{P}} \approx \Phi$. With reference to Fig. 8 c) and the $\mathcal{E}_{\mathcal{P}}$ definition (31), significant positive and negative contributions of this term span regions of strong acceleration and deceleration, respectively. This can be shown conceptually by invoking the TSL approximation which yields the following estimate: $\mathcal{E}_{\mathcal{P}} \approx -p_{G_e} \mathbf{V}_e \delta^{**}$. For typical adiabatic flows, $\delta^{**} > 0$ with the local density deficit being associated with thermo-compressible interference due to viscous self-heating, free-stream compressibility and local curvature variations. The implication is that the local $\mathcal{E}_{\mathcal{P}}$ magnitude and the corresponding peak value positions are determined by the trade-off between local flow acceleration/deceleration and sufficient δ^{**} growth, with higher AoA acting towards amplifying the $\mathcal{E}_{\mathcal{P}}$ contributions along the suction side whilst shifting the position of maximum $\mathcal{E}_{\mathcal{P}}$ closer to the leading edge. At about $x/c = 0.8$, the $\mathcal{E}_{\mathcal{P}}$ curves transition to negative values ($p_{G_e} > 0$) forming a pressure work defect "spike", with the minimum value being attained close to the trailing edge regardless of AoA and airfoil side considered.

This spike acts towards "flattening" the faster trailing edge $d\dot{\mathcal{E}}_{\mathcal{K}}/ds$ growth such that the net $\dot{\mathcal{E}}_{\mathcal{K}} + \dot{\mathcal{E}}_{\mathcal{P}}$ resembles the viscous dissipation evolution trends of Fig. 8 b). The numerical calculation of Φ is obtained from the $C_{\mathcal{D}}$ definition (34) such that $\Phi = \int \rho_e V_e^3 C_{\mathcal{D}} \, ds$. The relatively weak dependence of $C_{\mathcal{D}}$ on mild pressure gradients [26, 31] yields a largely invariant evolution of $C_{\mathcal{D}}$ along the suction side for $a \leq 6^\circ$ and an approximately AoA independent $C_{\mathcal{D}}$ behaviour along the pressure side, as shown in Fig. 9 a) and b). The superpositioned cyan dashed line is obtained by Sato's [26] turbulent flat plate dissipation coefficient $C_{\mathcal{D}_{FP}}$ expression (assuming smooth surface) and confirms that in the absence of substantial acceleration and deceleration, the $C_{\mathcal{D}}$ evolution is approximately Reynolds dependent

($Re_x = \rho_\infty V_\infty x \mu_\infty^{-1}$) and roughly equal to that of a flat plate. Thus, the local dissipative contributions are primarily controlled by the intensity of the local flow acceleration and deceleration via the $\rho_e V_e^3$ factor meaning that higher AoA values result in more "concave-shaped" and "linear-shaped" dissipation evolutions over the airfoil suction and pressured sides, respectively. The above have a direct implication on how the dissipation is distributed along the flow path, with higher AoA flows progressively shifting a larger fraction of the total upper side dissipation on the airfoil boundary layers and vice versa for the pressure side. Larger $\Phi_{\text{wake}}/DV_\infty$ values are desirable for BLI propulsion because this ratio represents a potential for energy recovery [18] that could be strategically utilized by the propulsion system for improved aerodynamic performance.

For this subsonic flow scenario, compressibility is negligible such that the affiliated baroclinic power is a higher order effect, as shown in Fig. 8 d). For $a = 0$, the baroclinic power behaves as a power sink ($\mathcal{B} > 0$) and grows monotonically at a progressively slower rate up to the airfoil's midbody whereafter a plateau region follows that terminates with a marginal spike close to the trailing edge. These qualitative characteristics are largely retained for the suction side regardless of AoA, with higher values of the latter merely amplifying the local $\mathcal{B}$ magnitude. Strong negative $\mathcal{B}$ contributions only manifest just downstream of the leading edge ($x/c \approx 0.05$), indicating the possibility of compressibility effects locally acting as a power source that partially negates its downstream loss contributions. Whereas local $\mathcal{B} < 0$ contributions are not explicitly precluded from the baroclinic power definition (29), the affiliated numerical challenge of postprocessing flow quantities such as $\nabla \cdot \mathbf{V}_e$ over regions of abrupt change in fluid properties involves a degree of uncertainty. The progressively higher growth rate $d\mathcal{B}/ds$ downstream of the suction side leading edge of higher AoA flows indicates that baroclinic loss generation dominates along overspeed regions due to dissipative heating effects of the boundary layer being more pronounced relative to the aft portion of the airfoil and the wake.

An important feature of the $\mathcal{B}$ evolution is that the wake region carries (approximately) no baroclinic power, $\mathcal{B}_{\text{wake}} \approx 0$, due to the viscous decay of the wake velocity pertubations (and thus viscous self-heating) at nearly constant pressure. Thus, the only relevant wake loss mechanism is viscous dissipation whereas the total baroclinic power loss $\mathcal{B}_\infty$ is generated upstream of the trailing edge such that $\mathcal{B}_\infty \approx \mathcal{B}_{\text{BL}}$. This observation confirms the validity of the arguments by Lamprakis et al. [19, 40] in obtaining an approximate baroclinicity-corrected $\mathcal{PER}$ factor of unpowered bodies assuming that $\mathcal{B}_{\text{wake}} \approx 0$. The actual accuracy of the $\mathcal{B}$ term will be addressed in the following subsection, as well as alternative means of approximating it.

The evolution of the total mechanical losses of the NACA0012 airfoil, as obtained from the left and right hand side terms of the defect mechanical balance (27), is shown in Fig. 10 at the same Re_c and M_∞ numbers and three AoA. For visual aid purposes, the shaded red area indicates a reference error ϵ with respect to the Φ^* curve. Comparison of the trends indicates that the relative error between the surface and volume integral forms of Φ^* is sensitive to AoA, with higher values of the latter resulting in more pronounced deviations. These are primarily associated with the numerical underestimation of the $\mathcal{B}$ component (to be addressed in the following subsection) and secondarily with the EIF and

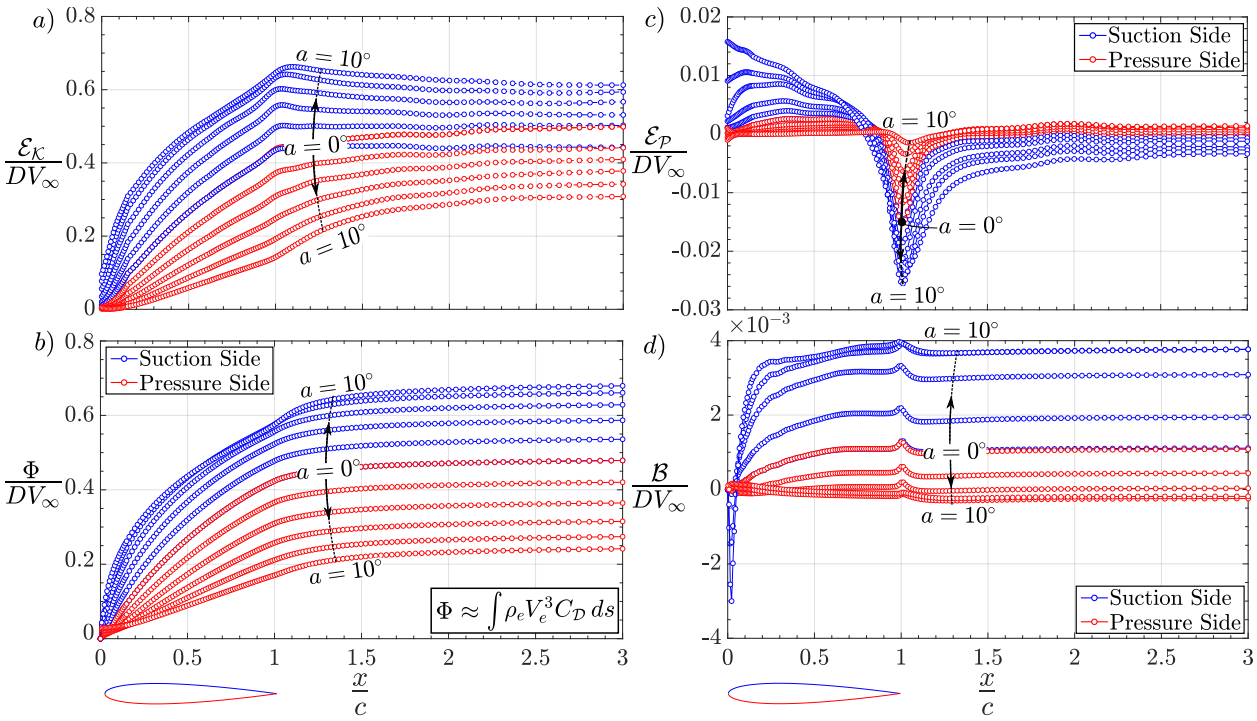


Fig. 8 Evolution of drag power-normalised defeect mechanical energy components for NACA0012 airfoil suction and pressure surfaces at $Re_c = 1 \times 10^6$, $M_\infty = 0.3$ and $a = 0°, 2°, 4°, 6°, 8°, 10°$.

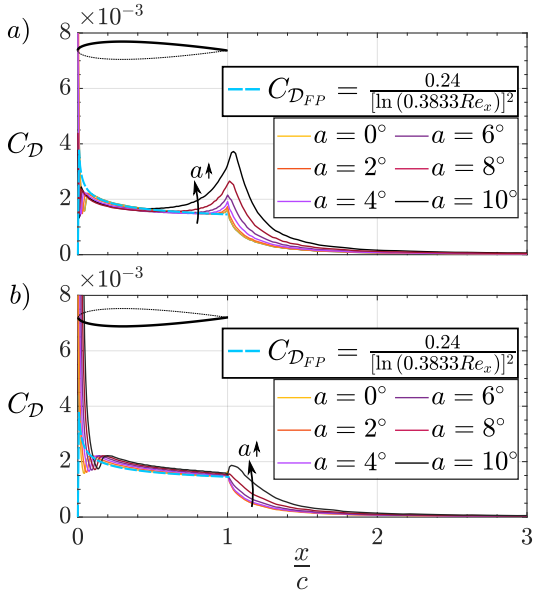


Fig. 9 $C_\mathcal{D}$ evolution of a NACA0012 airfoil at $Re_c = 1 \times 10^6$, $M_\infty = 0.3$ and $a = 0°, 2°, 4°, 6°, 8°, 10°$: a) Suction Side b)Pressure Side. The cyan curves show the $C_{\mathcal{D}_{FP}}$ expression for a smooth turbulent flat plate by Sato [26].

RVF flow alignment assumption used in the derivation. The dependence of both $\mathcal{E}_\mathcal{K}$ and $\mathcal{E}_\mathcal{P}$ on edge quantities implies that miscalculation of the latter may compromise the accuracy of their mechanical loss predictions. This results in an underestimation of the losses from the $\mathcal{E}_\mathcal{K} + \mathcal{E}_\mathcal{P}$ term in the wake region for all AoA scenarios due to the gradual mesh

coarsening and to a circumstantial overestimation on the airfoil surfaces for the upper AoA regime due to the additional RVF and EIF flow alignment assumptions of the derivation. On the other hand, the respective volume integral form of Φ^* with $\mathcal{B} \approx 0$ is independent of edge quantities[††] and nearly invariant to minor miscalculations of the boundary layer thickness due to the dissipative contributions of the boundary layer being confined close to the wall (typically for turbulent boundary layers).

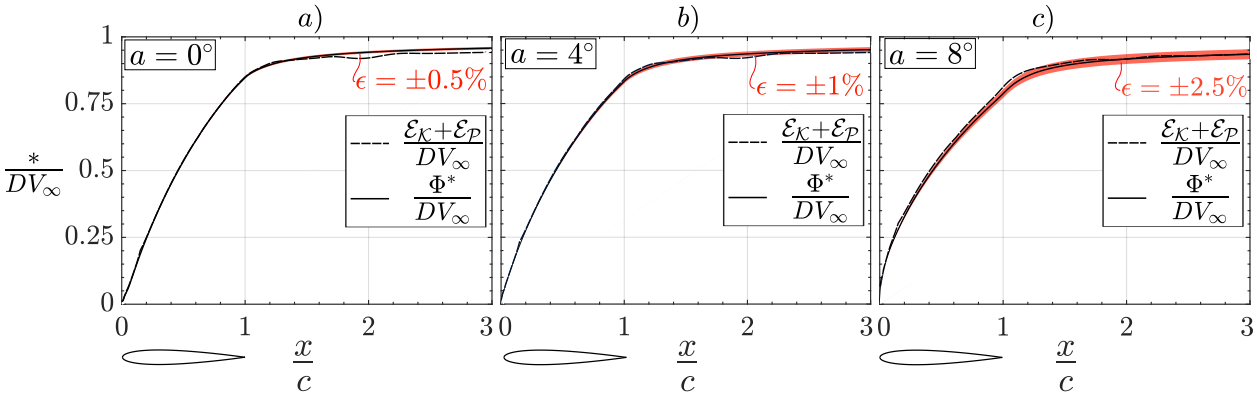


Fig. 10 Drag power-normalised mechanical loss evolution of a NACA0012 at $Re_c = 1 \times 10^6$, $M_\infty = 0.3$ and varying a, as obtained from $\mathcal{E}_\mathcal{K} + \mathcal{E}_\mathcal{P}$ and Φ^*.

E. Accuracy of Baroclinic Power

In assessing the accuracy of the baroclinic power definition (29), its asymptotic value is compared against the baroclinic residual Θ_∞, as obtained from the integration of Θ over a fully expanded domain enclosing the aerodynamic body. For further verification purposes, Sato's baroclinic power expression (49) and its approximation, defined as the difference between the baroclinicity-corrected dissipation (50) and $\Phi = \int \rho_e V_e^3 C_\mathcal{D}\, ds$, are also plotted for reference in Fig. 11 a) - j) for various operating conditions. As discussed earlier, the $\mathcal{B}$ and $-\Pi_V$ definitions do not represent physically the same quantity, because the $-\Pi_V$ derivation lumps the -$\mathcal{E}_\mathcal{P}$ contributions. However, the latter term rapidly decays downstream of the trailing edge, such that the notions of $-\Pi_V$ and $\mathcal{B}$ coincide. Thus, the various terms are primarily benchmarked based on their deviation from the asymptotic Θ_∞ value as per Eq. (38) by noting that Θ_∞ may also be subject to numerical uncertainties. Sato's exact $-\Pi_V$ term (49) provides numerically the most consistent predictions for all adiabatic flow scenarios (see Fig. 11) a) - f)) tested and accurately captures the baroclinic power excess affiliated with increasing M_∞ and AoA. Notice that higher M_∞ numbers tend to shift the $-\Pi_V$ curves upwards whereas increasing the AoA leads to more "concave-shaped" $\mathcal{B}$ and $-\Pi_V$ distributions, indicating a progressive shift of the baroclinic loss generation closer to the leading edge, in agreement with the discussion of the previous subsection. Overall, the approximate $-\Pi_V$ and $\mathcal{B}$ definitions tend to substantially underestimate the baroclinic residual power, with the validity of the former term being subject to its derivation assumptions and the accuracy of the latter being largely

[††]The $\rho_e V_e^3$ factor of the Φ expression (35) self-cancels with the denominator of the $C_\mathcal{D}$ definition (34).

dependent on the inaccurate numerical calculation of the $\nabla \cdot \mathbf{V}_e$ integrand.

Figure 11 g) - i) shows that wall cooling and heating are affiliated with significant negative and positive baroclinic contributions of up to $\Theta_\infty \approx 18\%$ for the extreme $T_w/T_\infty = 3$ scenario. These contributions are only adequately captured by the exact $-\Pi_V$ and $\mathcal{B}$ formulations whereas the approximate expression is invalid for non-adiabatic walls. The sign change with wall cooling and heating signifies the duality of the baroclinic power acting as a power source ($\mathcal{B} < 0$) and a power sink ($\mathcal{B} > 0$) for heat absorption and heat deposition, respectively. For typical adiabatic flows, the baroclinic losses ($\mathcal{B} > 0$) due to the self-heating of the boundary layer are small and commonly incorporated as a correction in the dissipation [20, 22].

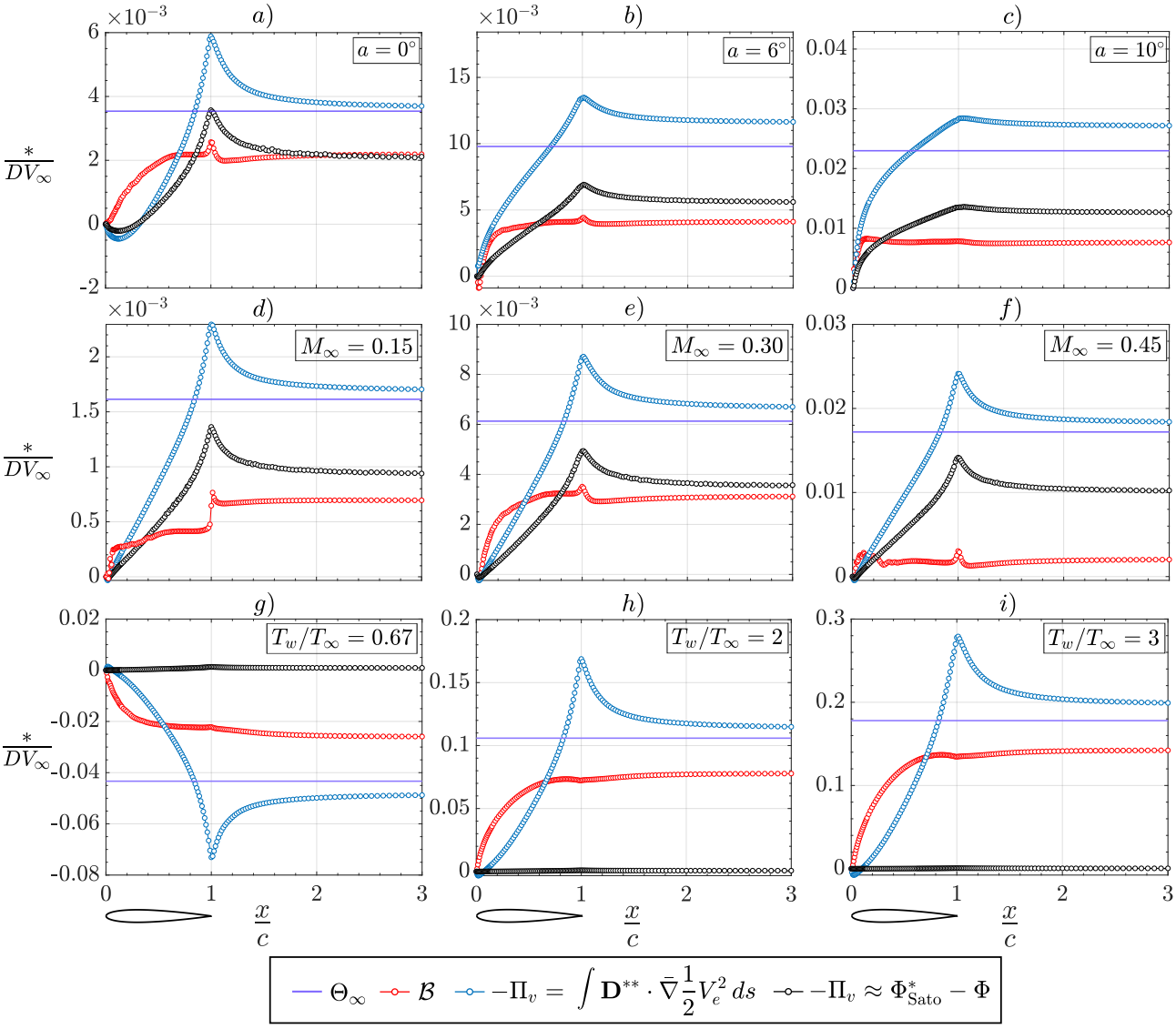


Fig. 11 Residual baroclinic power expression comparison for a NACA0012 at fixed: a) - c) $Re_c = 1 \times 10^6$, $M_\infty = 0.3$. d) - f) $Re_c = 1 \times 10^7, a = 4°$ g) - i) $Re_c = 1 \times 10^7, M_\infty = 0.15, a = 4°$.

V. Viscous Mechanical Energy Generation

The previous defect formulations were carried out in the RRF where the free stream flow passes over a stationary aerodynamic body. In capturing the viscous mechanical energy generation mechanisms associated with the motion of the airframe surfaces and their correlation with the defect force definition, a conversion to the ARF is required. This is achieved via a Galilean transformation (see examples in [19, 25]) between relative and absolute reference frames. The two are related via the following velocity relation:

$$\mathbf{V}_{\mathrm{A}} = \mathbf{V} - \mathbf{V}_{\infty} \tag{51}$$

where $\mathbf{V}_{\mathrm{A}}$ the ARF velocity vector as perceived from a coordinate system fixed in space. For an aircraft flying through quiescent atmosphere, its ARF velocity is merely opposite to the conventional free-stream RRF velocity vector , i.e $\boldsymbol{V}_{\mathrm{A}_F} = -\boldsymbol{V}_{\infty}$.

A. Formulation

Forming the dot product of the defect momentum equation with the free-stream velocity vector yields:

$$\oiint (\boldsymbol{V}_e \rho_e \boldsymbol{V}_e \cdot \boldsymbol{V}_{\infty}) \cdot \hat{\boldsymbol{n}}\, d\mathcal{S}^* - \oiint (\boldsymbol{V} \rho \boldsymbol{V} \cdot \boldsymbol{V}_{\infty}) \cdot \hat{\boldsymbol{n}}\, d\mathcal{S} = -\oiint p_e \boldsymbol{V}_{\infty} \cdot \hat{\boldsymbol{n}}\, d\mathcal{S}^* - \oiint [-p\boldsymbol{V}_{\infty} \cdot \hat{\boldsymbol{n}} + \bar{\bar{\boldsymbol{\tau}}} \cdot \hat{\boldsymbol{n}} \cdot \boldsymbol{V}_{\infty}]\, d\mathcal{S} \tag{52}$$

Subtraction of (52) from (25) and use of the following identities:

$$\oiint p_e \boldsymbol{V}_{\mathrm{A}_e} \cdot \hat{\boldsymbol{n}}\, d\mathcal{S}^* - \oiint p \boldsymbol{V}_{\mathrm{A}} \cdot \hat{\boldsymbol{n}}\, d\mathcal{S} = \oiint p_{G_e} \boldsymbol{V}_{\mathrm{A}_e} \cdot \hat{\boldsymbol{n}}\, d\mathcal{S}^* - \oiint p_{G_e} (\boldsymbol{V}_{\mathrm{A}}) \cdot \hat{\boldsymbol{n}}\, d\mathcal{S} + \iiint p_{\infty} \nabla \cdot \boldsymbol{V}_e\, d\mathcal{V}^* - \iiint p_{\infty} \nabla \cdot \boldsymbol{V}\, d\mathcal{V} \tag{53}$$

$$\frac{(\boldsymbol{V}_e - \boldsymbol{V})^2}{2} = \frac{V_e^2 + V^2}{2} - (\boldsymbol{V} \cdot \boldsymbol{V}_e) = \frac{V_e^2 - V^2}{2} + \boldsymbol{V} \cdot (\boldsymbol{V} - \boldsymbol{V}_e) \tag{54}$$

yields the integral form of the viscous energy generation imparted to the flow:

$$\iint \frac{(\boldsymbol{V}_e - \boldsymbol{V})(\boldsymbol{V}_{\mathrm{A}} + \boldsymbol{V}_{\mathrm{A}_e})}{2} \rho \boldsymbol{V} \cdot \hat{\boldsymbol{n}}\, d\mathcal{S}_{\mathrm{TP}} = \iint \left[p_G \boldsymbol{V}_{\mathrm{A}} - p_{G_e} \boldsymbol{V}_{\mathrm{A}_e} \right] \cdot \hat{\boldsymbol{n}}\, d\mathcal{S}_{\mathrm{TP}} + \iint p_{G_e} \boldsymbol{V}_{\mathrm{A}_e} \cdot \hat{\boldsymbol{n}}\, d\mathcal{S}_{\mathrm{TP}}^{\delta^*} - \iiint \left[p_{G_e} \nabla \cdot \boldsymbol{V}_e - p_G \nabla \cdot \boldsymbol{V} \right] d\mathcal{V} - \iiint p_{G_e} \nabla \cdot \boldsymbol{V}_e\, d\mathcal{V}^{\delta^*} + \iiint (\bar{\bar{\tau}} \cdot \nabla) \cdot \boldsymbol{V}\, d\mathcal{V} - \oiint \bar{\bar{\tau}} \cdot \boldsymbol{V}_{\mathrm{A}} \cdot \hat{\boldsymbol{n}}\, d\mathcal{S} \tag{55}$$

where $\boldsymbol{V}_{\mathrm{A}_e} = \boldsymbol{V}_e - \boldsymbol{V}_\infty$, the ARF edge velocity vector. Rearrangement of Eq. (55) yields the viscous mechanical energy generation balance for an aerodynamic body flying through quiescent atmosphere:

$$\mathcal{F}_D V_\infty = \widetilde{\mathcal{E}}_k + \widetilde{\mathcal{E}}_p + \widetilde{\mathcal{E}}_\tau + \mathcal{B} + \Phi \tag{56}$$

where the left-hand side term $\mathcal{F}_D V_\infty$ measures the upstream nearfield defect drag power transmitted to the flow via the body's walls. The right-hand side captures its farfield manifestation inside the shear layers, in the form of excess viscous mechanical energy outflows and volumetric losses. All the terms are defined hereafter:

The nearfield viscous defect drag power generation $\mathcal{F}_D V_\infty$,

$$\mathcal{F}_D V_\infty = \iint p_G \boldsymbol{V}_\infty \cdot \hat{\boldsymbol{n}} - (\bar{\bar{\tau}} \cdot \boldsymbol{V}_\infty) \cdot \hat{\boldsymbol{n}} \, d\mathcal{S}_{\mathrm{B}} - \iint p_G \boldsymbol{V}_\infty \cdot \hat{\boldsymbol{n}} \, d\mathcal{S}_{\mathrm{B}^*} \tag{57}$$

This is the accumulated defect drag power imparted to the flow from the airframe surfaces flying at a finite velocity $-\boldsymbol{V}_\infty$ through quiescent atmosphere. It measures individual contributions from the integrated skin friction forces along the real body surfaces (skin friction drag generation) and the difference between the integrated pressure forces acting over the real and fictitious bodies which persists in the wake (pressure drag generation). This term traces the local generation of the defect drag power for partially enclosed wall surfaces, as well as the total viscous drag power for a Trefftz plane positioned at a wake position that ensures the alignment of the effective wake body surfaces with the free-stream flow direction.

The viscous kinetic energy excess rate $\widetilde{\mathcal{E}}_k$,

$$\widetilde{\mathcal{E}}_k = \iint \frac{(\boldsymbol{V} - \boldsymbol{V}_e)(\boldsymbol{V}_{\mathrm{A}} + \boldsymbol{V}_{\mathrm{A}_e})}{2} \rho \boldsymbol{V} \cdot \hat{\boldsymbol{n}} \, d\mathcal{S}_{\mathrm{TP}} \tag{58}$$

This is the non-isentropic component of the kinetic energy flow rate crossing the Trefftz plane due to the viscous entrainment of the wall-adjacent fluid layers. Thus, the walls of an aerodynamic body associated with finite flight velocity $-\boldsymbol{V}_\infty$ supply viscous kinetic power to the flow which is then deposited and attenuated via viscous dissipation inside the wake. To the extent that $\boldsymbol{V}_e \simeq \boldsymbol{V}_\infty$, such as in a zero pressure gradient viscous flow (flat plate) or a free shear layer, the kinetic energy excess characteristics are driven by viscosity alone, and Eq. (58) asymptotes to the axial kinetic energy term E_a of the power balance [17] as well as the flat plate mean streamwise kinetic energy term of Renard and Deck [25].

The viscous pressure work rate $\widetilde{\mathcal{E}}_p$,

$$\widetilde{\mathcal{E}}_p = \iint p_G \boldsymbol{V}_{\mathrm{A}} - p_{G_e} \boldsymbol{V}_{\mathrm{A}_e} d\mathcal{S}_{\mathrm{TP}} + \iint p_{G_e} \boldsymbol{V}_{\mathrm{A}_e} \, d\mathcal{S}_{\mathrm{TP}}^{\delta^*} \tag{59}$$

This is the viscous or entropic component of the pressure work rate acting on the defect flow exiting from the Trefftz plane. Positive contributions of this term span accelerative flow regions of the body (such as the vicinity of the leading edge) whereas substantial negative contributions (via the second term) manifest along compressive regions with large viscous displacement, such as the aft region of airfoils or fuselages as well as the semi-expanded near wake region. As a result, this term acts towards negating large viscous kinetic energy excess contributions along adverse pressure gradient zones.

B. Test Cases

The evolution of the viscous kinetic energy and pressure work components of the balance (56), normalised by the nearfield drag power DV_∞, is plotted in Fig. 12 a) and b) for the suction and pressure sides of a NACA0012 airfoil at fixed $Re_c = 1 \times 10^6$, $M_\infty = 0.3$ and 6 AoA. Strong $\widetilde{\mathcal{E}}_k < 0$ and $\widetilde{\mathcal{E}}_k > 0$ contributions are spanning, locally, accelerative and decelerative zones of the suction side respectively, with their magnitude being further amplified by higher AoA. The perplexing negative sign of the kinetic energy evolution along the near leading edge indicates work expenditure from the flow and seems to run counter to the strictly positive excess kinetic energy arguments of the RVF power balance. In other words, the negative $\widetilde{\mathcal{E}}_k$ indicates that the pressure field is the driving mechanism that sustains this (negative) kinetic energy growth via the substantial $\widetilde{\mathcal{E}}_p > 0$ contributions, as indicated by Fig. 12 b). The opposite applies to the strong adverse pressure gradient zone at the aft portion of the airfoil, where the substantial viscous kinetic energy supplied to the boundary layer is partially balanced by strong negative $\widetilde{\mathcal{E}}_p$ contributions. In the limit of a zero-pressure gradient or a small pertubation flow, where the pressure field variations are typically small such that $\widetilde{\mathcal{E}}_p \approx 0$. For these flow scenarios, $\widetilde{\mathcal{E}}_k$ measures the kinetic energy gain ($\widetilde{\mathcal{E}}_k > 0$) that is supplied by the relative movement of the walls to the boundary layer via the action of viscosity. This is the case for the airfoil's pressure side at higher AoA for which the $\widetilde{\mathcal{E}}_k$ evolution behaves similar to the E_a term of the power balance and is strictly positive along the flow path. Downstream of the trailing edge, the rapid decay of the body's pressure field manifests as a sharp reduction in $\widetilde{\mathcal{E}}_p$ which is followed by the viscous decay of $\widetilde{\mathcal{E}}_k$ via dissipation[‡‡].

The above imply that the notions of $\widetilde{\mathcal{E}}_k$ and $\widetilde{\mathcal{E}}_p$ are typically coupled and subject to mutual energy transfer exchanges due to the pressure-velocity coupling. In tracing the actual viscous energy excess transmitted to the flow from the flying body, one should consider the net viscous mechanical energy excess $\widetilde{\mathcal{E}}_{\text{mech}} = \widetilde{\mathcal{E}}_k + \widetilde{\mathcal{E}}_p$[§§] evolution instead, as shown in Fig. 12 c). The resulting $\widetilde{\mathcal{E}}_{\text{mech}}$ curve accumulates at a progressively slower rate up to $x/c \approx 0.8$ whereafter the change in monotonicity $d(\widetilde{\mathcal{E}}_{\text{mech}})/dx$ terminates at the trailing edge with a local minimum. A nearly identical behaviour is reported by Aguirre [35] via his velocity decomposition method [36]. To the authors' opinion, this minimum originates primarily from the invalidity of the EVF and EIF alignment assumption (see Sec. II.C) for flows with non-marginal

[‡‡]This is strictly true only for a fully-expanded flow, where the pressure field does not affect $\widetilde{\mathcal{E}}_k$ changes.

[§§]$\widetilde{\mathcal{E}}_\tau$ is omitted due to being negligible relative to the other two terms.

viscous displacement and secondarily from the excess $\widetilde{\mathcal{E}}_p$ expended by the flow to "overcome" the strong adverse pressure gradient zone along the aft portion of the airfoil. Downstream of the trailing edge, the semi-expanded wake region is affiliated with a short $\widetilde{\mathcal{E}}_{\text{mech}}$ rise prior to its final viscous decay at nearly constant pressure, i.e. $\widetilde{\mathcal{E}}_p \approx 0$ along the fully-expanded wake region. The latter statement implies that in the absence of pressure gradients, $V_e = V_\infty$ and the wake's viscous mechanical energy excess reduces to the conventional RVF excess kinetic energy term [17, 18] in agreement with the argument of Sec. IV.B.3.

From a wake energy recovery perspective, the net viscous mechanical energy $\widetilde{\mathcal{E}}_k + \widetilde{\mathcal{E}}_p$ closely resembles the baroclinicity-corrected potential for energy recovery factor, $\mathcal{PER} = 1 - (\Phi + \Theta_\infty)/DV_\infty$, [19] relevant for BLI propulsion. This is evident by rearranging Eq. (56):

$$\frac{\widetilde{\mathcal{E}}_{\text{mech}}}{\mathcal{F}_D V_\infty} = 1 - \frac{\Phi^*}{\mathcal{F}_D V_\infty} \tag{60}$$

where the right-hand side of Eq. (60) differs from $\mathcal{PER}$ in that the defect drag is used in the denominator. The comparison between $\widetilde{\mathcal{E}}_{\text{mech}}$ and the conventional $\mathcal{PER}$ definition signifies that the discrepancy between the two is more pronounced in close proximity of the trailing edge, where the $\mathcal{PER}$ metric predicts larger recoverable energy estimations, with higher deviations being noted for increasing AoA. This discrepancy in the near wake ($1 < x/c < 1.4$) is partly a consequence of using DV_∞ as the denominator of $\widetilde{\mathcal{E}}_{\text{mech}}$ rather than $\mathcal{F}_D V_\infty$, as defined in Eq. (60). At a short distance downstream (about $x/c > 1.4$) however, $\mathcal{F}_D$ asymptotes to D (see Fig. 4 d)) such that Eq. (60) resembles $\mathcal{PER}$, resulting in good agreement between the two. Another source of uncertainty arises from the assumed flow alignment between the RVF and the EIF. This assumption becomes less accurate along regions of notable viscous displacement, such as the vicinity of the trailing edge of the airfoil.

1. Full Balance

The evolution of the viscous energy generation terms of Eq. (56) are shown in Fig. 13 for various operating conditions. The right-hand side consitutents of the balance indicate that $\mathcal{F}_D V_\infty$ physically measures, at each streamwise position, the upstream defect drag power transmitted to the flow, which manifests as the sum of the upstream mechanical losses Φ^* and the excess viscous mechanical energy outflow $\widetilde{\mathcal{E}}_{\text{mech}}$ generated inside the shear layers. The spatial evolution of $\widetilde{\mathcal{E}}_{\text{mech}}$ in Fig. 13 signifies physically the presence of a "defect power supply" and a "defect power deposition" zone. The former corresponds to the airframe surfaces and the near wake region where the viscous mechanical energy excess is accumulating (with the exception of the near trailing edge region) and terminates when $\mathcal{F}_D V_\infty$ asymptotes to the viscous drag power. The latter corresponds to the downstream wake region which accounts for the irreversible conversion of $\widetilde{\mathcal{E}}_{\text{mech}}$ into wake dissipation.

In the absence of strong heat transfer effects, Fig. 13 a) - f) indicate that the defect drag power generation

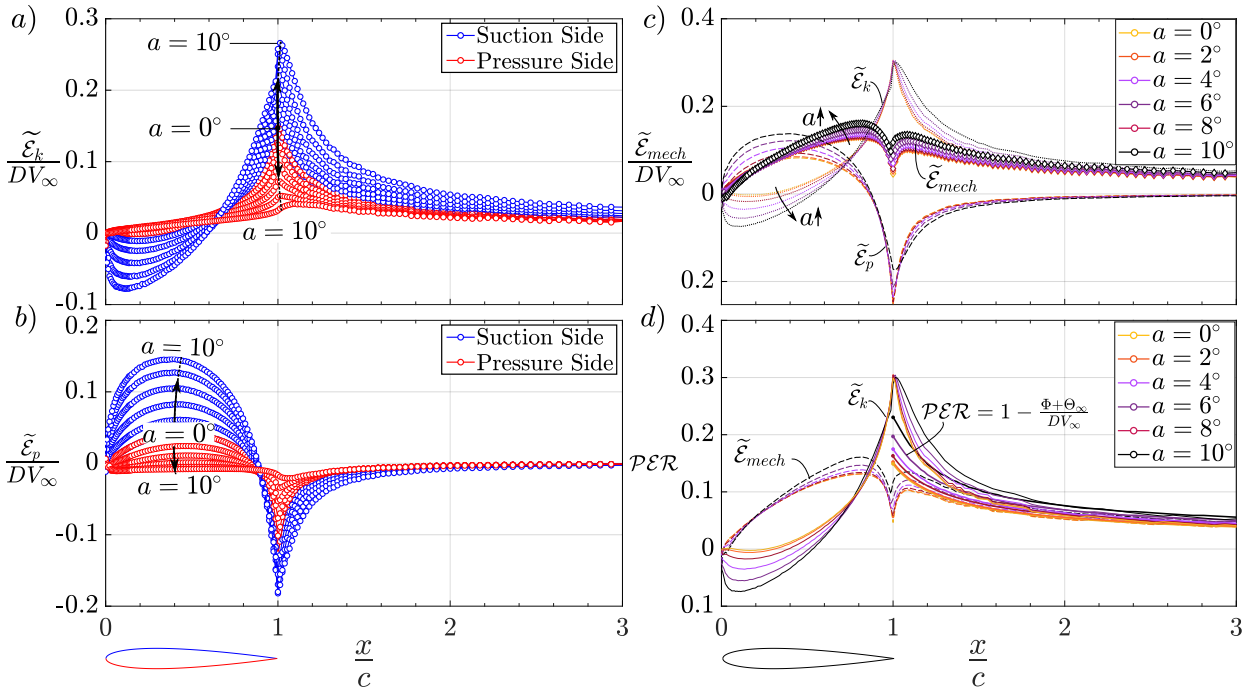


Fig. 12 Drag power-normalised viscous mechanical energy generation components for NACA0012 airfoil at $Re_c = 1 \times 10^6$, $M_\infty = 0.3$ and varying a.

process is primarily controlled by the viscous dissipation, with the remaining viscous mechanical energy excess and baroclinic power components measuring, typically, $< 15\%$ and $< 2\%$, respectively. For reference, the asymptotic $\mathcal{F}_D V_\infty$ value at $x/c = 2$ is shown in each of the subplots along with the corresponding $\mathcal{B}$ decrement relative to the Θ_∞ value,$(\Theta_\infty - \mathcal{B}_\infty)/DV_\infty$. Comparison between the two signifies that the accuracy of the $\mathcal{F}_D V_\infty$ evolution and its drag power estimation is strongly correlated to the numerical miscalculation of $\mathcal{B}$. This is evident by simply correcting $\mathcal{F}_D V_\infty$ for the missing baroclinic power, which results in drag power measurements within 1% for all adiabatic and non-adiabatic flows (see Fig. 13 h) -g)) scenarios tested. Notice that the underestimation of $\mathcal{B}$ and its subsequent correction is also valid for the RRF balance (27) terms of Fig. 10 a) -c), and results in improved matching between the left and right-hand side terms within 1%. For completeness, Table 1 presents the numerical values of nearfield drag coefficients[¶¶] (c_D) and their corresponding farfield defect drag coefficients ($c_{\mathcal{F}_D}$) at $x/c = 2$ for all flow conditions shown in Fig. 13 (a–g). The relative deviation between the two coefficients is also provided, demonstrating a close agreement of less than 4% for all cases.

[¶¶]The drag coefficients are obtained by normalising the corresponding drag force with $\frac{1}{2}\rho_\infty V_\infty^2 c$.

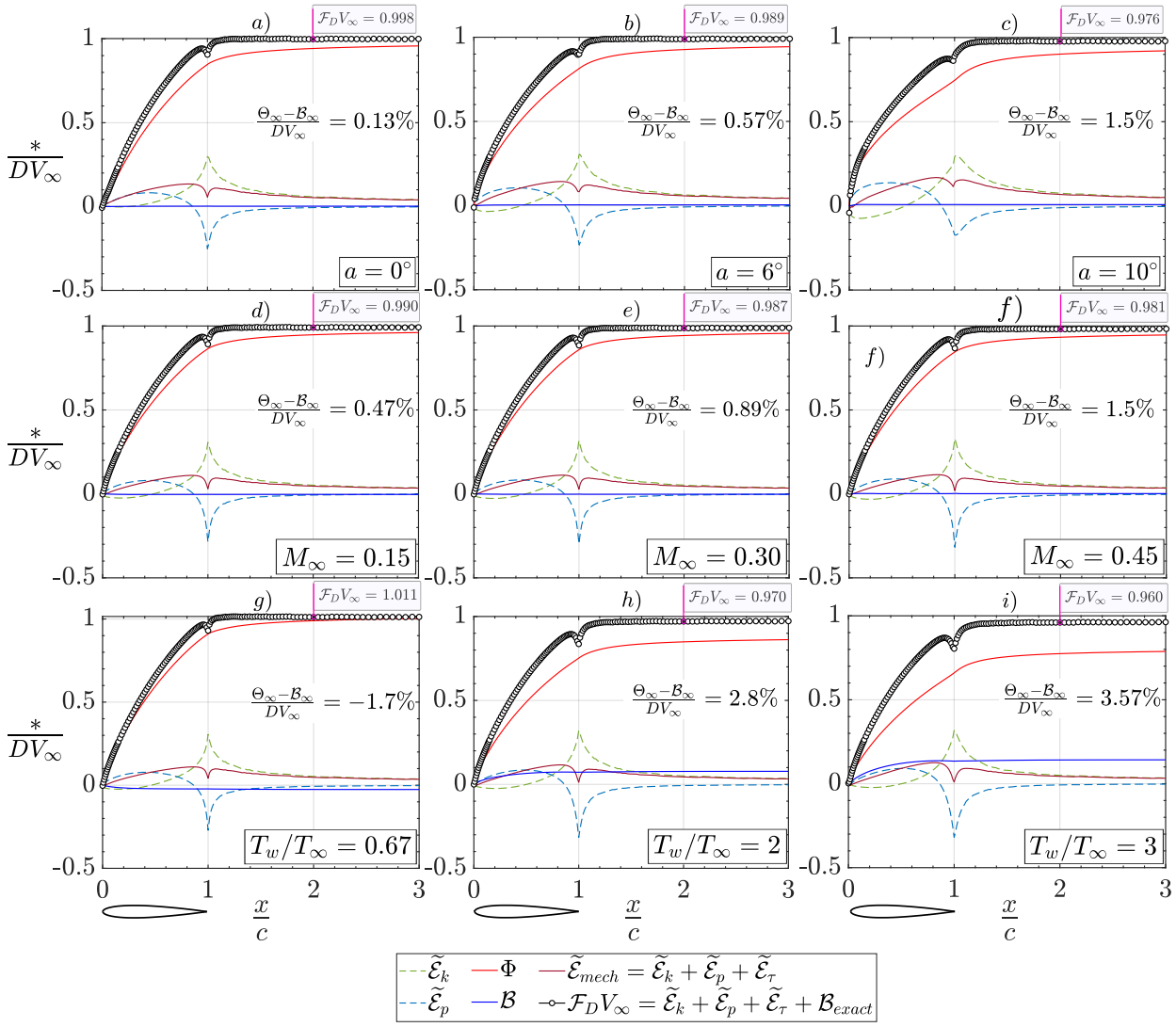


Fig. 13 Drag power-normalised viscous energy generation balance terms for a NACA0012 at fixed: a) - c) $Re_c = 1 \times 10^6$, $M_\infty = 0.3$ d) - f) $Re_c = 1 \times 10^7$, $a = 4°$ g) - i) $Re_c = 1 \times 10^7$, $M_\infty = 0.15$ and $a = 4°$.

Table 1 Nearfield viscous drag coefficient values (c_D) versus farfield defect drag coefficient ($c_{\mathcal{F}_D}$) predictions at $x/c = 2$ for the NACA0012 cases of Fig. 13.

Test case	a)	b)	c)	d)	e)	f)	g)	h)	i)
c_D	0.01085	0.01290	0.01816	0.00804	0.00809	0.00821	0.00856	0.00740	0.00730
$c_{\mathcal{F}_D}$	0.01083	0.01276	0.01772	0.00796	0.00798	0.00805	0.00865	0.00718	0.00701
$1 - \frac{c_{\mathcal{F}_D}}{c_D}$ (%)	0.2	1.1	2.4	1	1.3	1.9	-1.1	3	4

C. Velocity Decomposition Method

In sifting out the isentropic flow field pertubations, Aguirre [35, 36] carried out a notional breakdown of the RVF velocity field into a non-isentropic ($\bar{\boldsymbol{V}}$) and an isentropic part ($\boldsymbol{V}^*$), such that:

$$\boldsymbol{V} = \bar{\boldsymbol{V}} + \boldsymbol{V}^* \tag{61}$$

where the two velocity vectors are assumed to be aligned, in agreement with the assumptions of Sec. II.C. The inviscid flow field is subsequently reconstructed by invoking the compressible steady-state Bernoulli equation [42]:

$$\frac{p^*}{p_\infty} = \left[1 + \frac{\gamma - 1}{2} M_\infty^2 \left(1 - \frac{V^2}{V_\infty^2}\right)\right]^{\frac{\gamma}{\gamma-1}} \tag{62}$$

where p^* denotes the isentropic pressure field. With similar arguments to the thin shear layer approximation, and following the previous work by Meheut [43], Aguirre assumed nearly identical pressure fields for the isentropic and RVF such that $p^* \simeq p$ by neglecting viscosity-induced pressure field flactuations inside shear layers. Thus, the validity of the Bernoulli relation (62) effectively extends to the RVF by substituting $p^* \simeq p$, which then yields an expression for the isentropic velocity magnitude V^* as a function of local and free-stream thermodynamic quantities [36] :

$$V^* = V_\infty \sqrt{1 - \frac{2}{(\gamma - 1) M_\infty^2} \left[\left(\frac{P_t}{P_{t_\infty}}\right)^{\frac{\gamma-1}{\gamma}} \zeta - 1\right]} \tag{63}$$

where P_t the total pressure and ζ a non-dimensional isentropic parameter expressed in terms of the total temperature T_t as:

$$\zeta = 1 + \frac{\gamma - 1}{2} M_\infty^2 \left(1 - \frac{V^2}{V_\infty^2} \frac{T_{t_\infty}^2}{T_t}\right) \tag{64}$$

The velocity decomposition method was subsequently used by Aguirre [36] to obtain a modified exergy balance for accurate drag estimations based on limited wind-tunnel wake-plane measurements. This was achieved by subtracting the isentropic exergy flux contributions from Arntz et al. [37, 38] original RVF exergy formulation, thereby eliminating Trefftz plane exergetic pertubations affiliated with the outer potential flow. Applying this principle to the conventional RVF mechanical energy balance as derived by Sanders and Laskaridis [18] and denoting with $\bar{()}$ and $()^*$ the non-isentropic and isentropic mechanical energy outflow components, respectively, the following viscous balance is obtained:

$$\bar{D} V_\infty = \bar{\dot{\mathcal{E}}}_k + \bar{\dot{\mathcal{E}}}_p + \Phi + \bar{\Theta} \tag{65}$$

where the non-isentropic energy components are implicitly extracted by filtering the isentropic components from the RVF terms, $\bar{()} = () - ()^*$, such that:

$$\bar{\dot{\mathcal{E}}}_k = \mathcal{E}_k - \mathcal{E}_k^* = \iint \left[\left(\frac{\rho}{2} \boldsymbol{V}_A^2 \right) \boldsymbol{V} - \left(\frac{\rho}{2} \boldsymbol{V}_A^{*2} \right) \boldsymbol{V}^* \right] \cdot \hat{\boldsymbol{n}} \, d\mathcal{S}_{\mathrm{TP}} \tag{66}$$

$$\bar{\dot{\mathcal{E}}}_p = \mathcal{E}_p - \mathcal{E}_p^* = \iint p_G (\boldsymbol{V} - \boldsymbol{V}^*) \cdot \hat{\boldsymbol{n}} \, d\mathcal{S}_{\mathrm{TP}} \tag{67}$$

$$\bar{\Theta} = - \iiint p_G (\nabla \cdot \boldsymbol{V} - \nabla \cdot \boldsymbol{V}^*) \, d\mathcal{V} \tag{68}$$

where $\bar{D}$ the non-isentropic profile drag component. Close inspection of the velocity decomposition approach and matching terms: $\bar{D} V_\infty \rightarrow (57)$, $(59) \rightarrow (67)$ and $(29) \rightarrow (68)$ reveals that Aguirre [35] has implicitly carried out an approximate viscous energy generation analysis similar to Eq. (56) for a fully enclosed aerodynamic body. However, the accuracy of the non-isentropic energy terms relies on the wrongly perceived definition of the simple inviscid flow field, as is evident by the lower integration limit of the isentropic flux terms (66), (67), (68), lying on the real body's walls and thereby omitting the viscous displacement effect. Therefore, the validity of the velocity decomposition approach and its agreement with the present derivation is subject to the significance of the isentropic contributions associated with the displacement portion of the Trefftz plane. For instance, the viscous pressure work rate $\widetilde{\mathcal{E}}_p$ definition (59) coincides with $\bar{\dot{\mathcal{E}}}_p$ to the extent that $p \approx p_e$ and additionally:

$$\iint p_{G_e} (\boldsymbol{V}_e - \boldsymbol{V}_\infty) \cdot \hat{\boldsymbol{n}} \, d\mathcal{S}_{\mathrm{TP}}^{\delta^*} \simeq 0 \tag{69}$$

Thus, the reconstruction of the isentropic pressure field and the cancellation of the outer isentropic flow field pertubations in the velocity decomposition approach rely coincidentally on the correct EIF definition, whereas the simple inviscid flow contributions are subtracted from the RVF terms. The effect of these assumptions and a comparison between the present formulation and that of Aguirre [35] will be addressed in the next subsection.

D. Method Comparison

A sample comparison of the $\widetilde{\mathcal{E}}_k$ (58) and $\widetilde{\mathcal{E}}_p$ (59) definitions against the corresponding $\bar{\dot{\mathcal{E}}}_k$ (66) and $\bar{\dot{\mathcal{E}}}_p$ (67) terms of Aguirre's velocity decomposition method [35, 36] are summarized in Fig. 14 for various operating conditions. For all the flow parameters tested, the accelerative parts of the airfoil (typically $x/c < 0.8$) yield the most notable discrepancies, with the latter being magnified by an increase in AoA, as shown in Fig. 14 a). Contrarily, the decelerating shear layer flow along the aft part of the airfoil and the wake region show an excellent agreement for all the examined flow scenarios, typically within 2% and 0.5%, respectively. The deviations between the two approaches are mainly a corollary of the EIF contributions (omitted by Aguirre's approach) being typically more pronounced closer to the leading edge region.

The result is a proportional overestimation of the individual $\bar{\tilde{\mathcal{E}}}_k$ and $\bar{\tilde{\mathcal{E}}}_p$ magnitudes for all the examined flow scenarios, with their net effect partially self-cancelling when considering the net viscous mechanical energy excess outflow $\bar{\tilde{\mathcal{E}}}_{\text{mech}}$. This is mainly true for low AoA and high Re_c flows with marginal flow displacement, as shown in Fig. 14 c). For subsonic or weakly transonic flows, Fig. 14 b) signifies that the proper inclusion of the EIF terms yields a Mach number invariant $\bar{\tilde{\mathcal{E}}}_k + \bar{\tilde{\mathcal{E}}}_p$ evolution along the airfoil and the wake, in agreement with the $\mathcal{PER}$ wake analysis of axisymmetric bodies of Ref. [40]. From a numerical point of view, Aguirre's approach is advantageous for transonic flows with shock formation (see Fig. 14 b) and $M_\infty = 0.6$ curves) in that it does not require explicit extraction of boundary layer edge properties, which may be slightly miscalculated in close proximity of the shock wave. Finally, wall cooling and heating are explicitly captured by the viscous terms via their effect on boundary layer properties, and the flow displacement. Thus, the cooling-induced suppression of the $d\delta^*/ds$ growth leads to reduced EIF contributions, and thereby better agreement between the predictions of the two methods, and vice versa for heating.

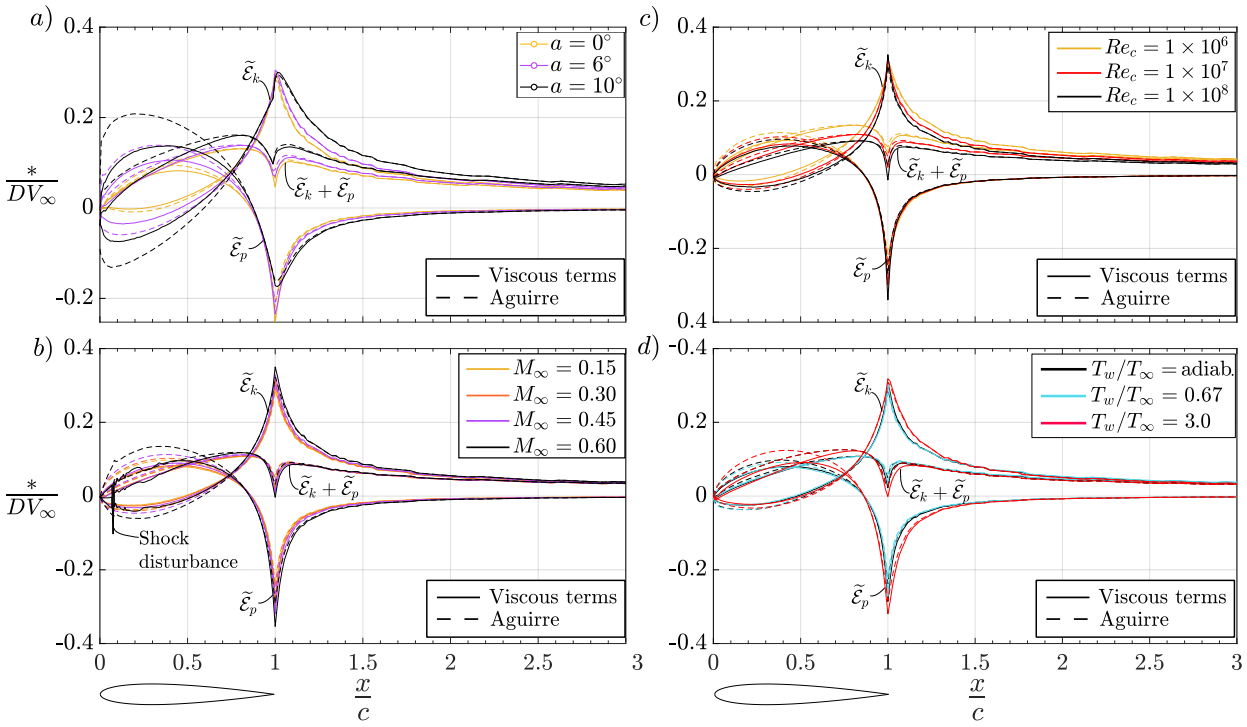


Fig. 14 Comparison of viscous mechanical energy generation flux components against Aguirre's [36] velocity decomposition method for a NACA0012 airfoil at fixed: a) $Re_c = 1 \times 10^6$, $M_\infty = 0.3$ b) $Re_c = 1 \times 10^7$, $a = 4°$ c) $M_\infty = 0.3$ $a = 4°$ d) $Re_c = 1 \times 10^7$, $M_\infty = 0.15$, $a = 4°$.

E. Application to Boundary Layer Ingestion Propulsion

As previously discussed, the sum $\widetilde{\mathcal{E}}_k + \widetilde{\mathcal{E}}_p$, when calculated along the airframe surfaces, represents the non-dissipated energy fraction transferred to the boundary layer as the aircraft moves through a quiescent atmosphere. The portion of the non-dissipated For conventional aircraft configurations without BLI propulsion (or for the unpowered NACA0012 airfoil examined herein), this energy is merely dissipated in the wake, increasing the power requirement by the aircraft engines. However, BLI propulsion offers the potential to strategically recover this energy, thereby reducing the power required for flight (see, for example, Refs. [17–19, 44]).

This energy recovery process is evaluated numerically for a 2D axisymmetric fuselage–BLI propulsor assembly. The propulsor is modelled as a Body Force Model (BFM) that replicates an actuator disk with a Boundary Layer Ratio (BLR) of BLR=0.5, meaning that it ingests half of the boundary layer height. The propulsor is located at the trailing edge and its "thrust"*** force is equal to half the drag of the unpowered fuselage and does not suffice to achieve a zero net assembly force. The remaining force imbalance on the fuselage-BLI propulsor assembly is assumed to be balanced by an external force, analogous to the isolated external force that is required for an "unpowered" body to reach dynamic equilibrium in the ARF, as explained by Sanders and Laskaridis [18]. More details on the numerical setup and the propulsor model are provided in Appendix A.

Figure 15 compares the evolution of the viscous mechanical energy terms $\widetilde{\mathcal{E}}_k$ and $\widetilde{\mathcal{E}}_p$[†††] for the BLI-powered axisymmetric fuselage against that of the same unpowered airframe at the same operating condition of $Re_c = 1 \times 10^6$ and $M_\infty = 0.6$. The energy recovery from the BLI propulsor manifests as an abrupt reduction in the wake's mechanical energy just downstream of it ($1 < x/c < 1.1$), thereby preventing the harvested energy from being deposited downstream as wake dissipation. A marginal reduction in $\widetilde{\mathcal{E}}_k + \widetilde{\mathcal{E}}_p$ persists after the BLI propulsor ($x/c > 1.1$), indicating that a small portion of the boundary layer energy has not been harvested.

Along the airframe surfaces, the aerodynamic interference of the BLI propulsor initiates at $x/c \approx 0.9$, resulting in a slight drop in the magnitude of $\widetilde{\mathcal{E}}_k$ and $\widetilde{\mathcal{E}}_p$. However, the viscous mechanical energy generation, measured by $\widetilde{\mathcal{E}}_k + \widetilde{\mathcal{E}}_p$, remains unaffected by the propulsor. This highlights the common misconception where BLI benefits are solely correlated with the kinetic energy of the boundary layer. Instead, the viscous pressure work rate largely balances any changes in $\widetilde{\mathcal{E}}_k$ associated with pressure gradients from aero-propulsive interference effects. It should be noted that the corresponding RVF mechanical energy flux terms (kinetic energy rate and pressure work rate) are only applicable in the wake region and contain compressibility-induced isentropic contributions in wake flow regions where $\Theta \neq 0$. Therefore, Θ must also be accounted for to cancel out isentropic compressibility effects to properly capture the potential for energy

***In the context of BLI propulsion, the concepts of thrust and drag are ambiguous. For clarity, the term 'thrust' is used here as a convenient way to denote the direction of the propulsive force.

†††All energy terms are normalised by the drag power, DV_∞, of the unpowered fuselage.

recovery, $\mathcal{PER}$ [18, 40] of an unpowered body. Therefore, $\widetilde{\mathcal{E}}_k$, $\widetilde{\mathcal{E}}_p$, and the defect derived $\mathcal{PER}$ forms of Eq. (60), act as a complimentary extension to the RVF energy methods, providing useful insights on aerodynamic interference effects. With reference to Fig. 15, the $\mathcal{PER}$ value at the trailing edge of the unpowered fuselage is ~ 0.11 which decreases to about 0.03 in the BLI-powered scenario. This represents a significant viscous energy recovery, corresponding to 8% of the bare airframe drag power. With reference to Fig. 15, the $\mathcal{PER}$ value at the trailing edge of the unpowered fuselage is ~ 0.11 which decreases to about 0.03 in the BLI-powered scenario. This represents a significant viscous energy recovery, corresponding to 8% of the bare airframe drag power.

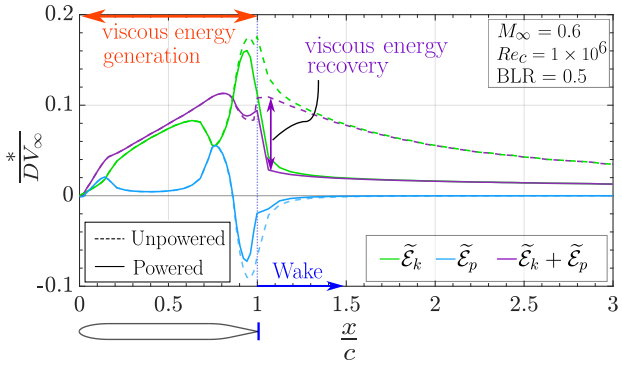


Fig. 15 Drag power-normalised viscous energy flux terms for an unpowered (dashed) and a BLI powered (solid) fuselage at $Re_c = 1 \times 10^6$ and $M_\infty = 0.6$.

VI. Conclusions

A defect integral analysis of the 2D steady-state compressible viscous flow about unpowered aerodynamic bodies has been derived in this paper from momentum and mechanical energy principles. The defect flow field has been obtained as the difference between the real viscous flow and the equivalent isentropic flow, thereby removing spurious force and work contributions from the flow field. The result is, first of their kind, formulations that are able to trace, quantify and causally relate local force production from the airframe surfaces to viscous (entropic) power transfer and generation mechanisms. This is achieved by introducing the definition of the defect force and its defect drag component as a physical measure of localised viscous drag and viscous power production, relevant for BLI propulsion. The viscous force-power generation process is shown to manifest along airframe surfaces and the near wake region whereafter it attains its final value that equals to the conventional viscous drag. In that sense, the formulations represent a coupled nearfield-farfield approach whereby the nearfield (viscous) defect drag power generation process is correlated with its farfield manifestation. Thereby, the defect formulations address the long-standing and inherent limitation of conventional farfield methods in providing any meaningful information about the upstream force-work production mechanisms. A useful property of the defect flow is that it is non-zero only within viscous regions, such that all the corresponding defect terms are obtained from physically intuitive volume and surface integrations of shear layer quantities and

parameters. This entails both numerical and experimental benefits because the integrations are now confined within the highly resolved regions of the computational and experimental domain. Additionally, the defect formulations are readily-compatible with existing energy/exergy-based formulations and therefore act as a complementary extension that enables the following:

1) Calculation and characterisation of the entropic part (baroclinic power) of the highly ambiguous volumetric pressure power term from Eq. (29) and its approximate inclusion in the power balance from Eq. (38).
2) Explicit and implicit estimation of the total viscous mechanical losses Φ^*, defined by the sum of viscous dissipation and baroclinic power, from their volume integral definitions (Eqs. (28) and (29)) and their surface integral representation (defect balance (27)), respectively. The latter offer a means of estimating the mechanical energy losses from limited wake experimental data for both adiabatic and non-adiabatic aerodynamic bodies.
3) A DVF-based definition of the $\mathcal{PER}$ metric from Eq. (60), relevant to energy recovery via BLI propulsion, along with an extension of its applicability to airframe surfaces. The energy recovery process from the BLI propulsor manifests as a reduction in the viscous mechanical energy, $\widetilde{\mathcal{E}}_k + \widetilde{\mathcal{E}}_p$ and mechanical losses, Φ^*, of the wake downstream of the propulsor.
4) Numerical and experimental estimation of the total viscous drag power and its upstream generation from integrations within the viscous domain for both adiabatic and non adiabatic flow scenarios.

In terms of limitations, the defect flow field definition is fundamentally applicable to flows across all Reynolds numbers. However, the final derivations rely on boundary layer assumptions that are more accurate at higher Reynolds numbers and in the wake region, which is largely independent of Reynolds number. These assumptions lose accuracy in regions where viscous displacement effects become significant, such as the aft body under strong adverse pressure gradients or flow separation. Furthermore, the formulations have been tested primarily under subsonic conditions, with only a single weak transonic flow case considered. As a result, the formulations have not been extensively tested for transonic flow scenarios, whereas the procedure outlined in Appendix E has not been numerically examined in this paper.

A. CFD Setup

A. NACA0012

The 2D CFD domain about the NACA 0012 airfoil along with relevant geometric features, boundary conditions and a partial mesh sample are summarized in Fig. A1. The NACA 0012 profile is obtained from NASA's polynomial expression for a chord length of unity and a sharp trailing edge (`https://turbmodels.larc.nasa.gov/naca0012_val.html`). The C-type numerical domain extends symmetrically about the airfoil chord line with velocity-inlet boundary conditions being imposed along the frontal elliptical arc and the divergent side line portions. The corresponding freestream velocity

components $\mathbf{V}_\infty = V_{\infty,x}\hat{x} + V_{\infty,y}\hat{y}$, are specified from the angle of attack, a, and the non-dimensional operating conditions, expressed in terms of the Re_c and M_∞ numbers. The elliptical arc is positioned at approximately $\mathrm{d}_{inlet} = 210 \times c$ from the airfoil leading edge whereas the vertical aft pressure outlet boundary plane of height $h_{outlet} = 600 \times c$ is located at $\mathrm{d}_{outlet} = 300 \times c$ downstream of the trailing edge.

Thereafter, numerical solutions of the Reynolds Averaged Navier-Stokes (RANS) equations are obtained from the commercial CFD solver FLUENT assuming fully-turbulent flow. Turbulence is modelled using the two-equation eddy-viscosity $\kappa - \omega$ SST model coupled with the Green-Gauss Cell-Based gradient scheme and second order spatial discretization. The air is modelled as an ideal gas with temperature-dependent properties according to a piece-wise polynomial fit, kinetic theory and Sutherland's law for the specific heat, thermal conductivity and fluid viscosity, respectively. The numerical domain is meshed as a structured C-type grid using the ANSYS ICEM CFD package and consists of $\sim 1 \times 10^6$ elements. The first cell height is adjusted for each operating condition to ensure the conformity of the mesh with the $y^+ < 1$ requirement of the turbulent model. A wall-normal growth ratio of 1.05 is selected to obtain high numerical resolution of the boundary layers and the near wake region. For the adiabatic airfoil studies, the thermal conductivity is kept constant and a kinetic theory-based temperature variation is imposed for cooled and heated walls. A uniform wall temperature ratio T_w/T_∞ is imposed for the non-adiabatic flow scenarios where the free-stream temperature is held constant throughout and equal to $T_\infty = 300$ C.

To evaluate the numerical accuracy of the grid, detailed mesh refinement and domain size studies have been conducted for a single flow condition corresponding to $Re_c = 1 \times 10^6$, $M_\infty = 0.15$ and $\alpha = 10°$, following the procedure outlined by Celik et al. [45]. Nine meshes have been evaluated, covering three domain sizes and three levels of mesh density for each domain size. The Grid Convergence Index (GCI) for the airfoil drag coefficients is found to be less than 0.1%, whether calculated via nearfield force integration or its farfield equivalent using mechanical energy conservation [17, 18]. Comprehensive grid convergence studies, along with further verification and validation of the computed drag and lift coefficients of the NACA0012 against data from Jespersen et al. [46], are documented in Refs. [47, 48] and are omitted here for brevity.

B. BLI Powered Axisymmetric Fuselage

A 2D cutaway of the axisymmetric fuselage-BLI propulsor CFD domain along with relevant geometric features, boundary conditions and a partial mesh sample are shown in Fig. A1. The fuselage shape consists of an elliptical nose, a cylindrical midbody, and a conical aftbody. It has a chord length of $c = 37.6$ m and a Fineness Ratio (FR) of FR = 12, defined as the ratio of the fuselage chord length to the midbody diameter. A pressure far field condition is imposed along all the control volume surfaces except for the vertical downstream plane, where a pressure outlet boundary condition is specified. The pressure far field boundary conditions are located at $d_{\text{farfield}} = 30 \times c$ from the fuselage and the pressure outlet boundary at $d_{\text{outlet}} = 80 \times c$. The numerical setup is identical to that of the NACA0012 and a similar refinement

strategy has been adopted near the walls and in the wake region, with a wall-normal growth ratio of 1.05 and a first height such that $y^+ < 1$, resulting in a total cell count of $\sim 8 \times 10^5$. Further details on the overall mesh refinement strategy and numerical uncertainty are provided in Refs. [40, 49] and are omitted here for brevity.

The BLI propulsor is positioned at the trailing edge of the fuselage and is modelled as a single-column cell zone. A constant x-momentum body force per unit volume, f_x, and its associated energy source term equal to $f_x V_x$ are applied to each cell of the propulsive domain. This setup is adopted from Refs. [19, 49, 50] and replicates an actuator disk [19, 50]. The magnitude of f_x is calibrated so that the net force on the BLI propulsor–fuselage assembly equals half the drag of the unpowered fuselage. The propulsor diameter is adjusted to ingest half of the boundary layer thickness, yielding BLR = 0.50.

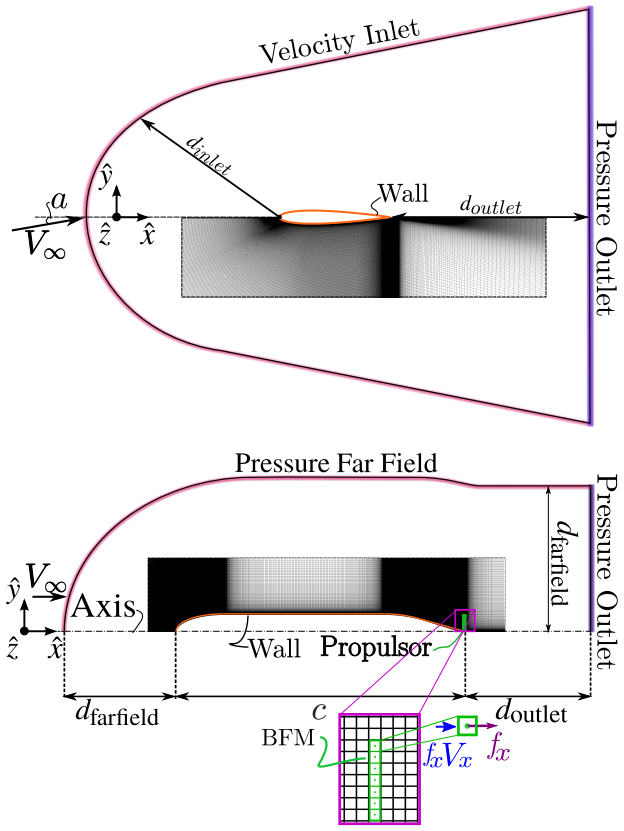


Fig. A1 2D CFD domain of NACA 0012 airfoil (upper) and 2D axisymmetric domain of fuselage - BLI propulsor assembly (lower) with annotated geometric features, boundary conditions and partial mesh sample.

B. Post-processing of Shear Layer Quantities

A. Boundary Layer Extraction

The shear layer thickness distribution $\delta(s)$ is numerically identified as the iso-surface (line for 2D) corresponding to a negligible total pressure deficit [40], such that ξ asymptotes to unity:

$$\xi = \frac{P_t}{P_{t_\infty}} \rightarrow 1 \tag{B1}$$

where P_t is the total pressure for a given ξ. The exact value of ξ depends on the quality of the numerical solution (convergence, high mesh density) and requires some manual fine-tuning to ensure the optimal balance between adequate inclusion of the viscous regions and exclusion of domain portions of marginal numerical dissipation. For the present studies, a threshold value of $\xi \approx 0.9996$ has been used throughout.

B. Shear Layer Quantities

The various shear layer quantities are calculated at each plane positions with respect to the local $s-n$ coordinate system normal to the wall and the trailing edge streamline as per Fig 1. The corresponding shear layer edge quantities are readily obtained from the flow field data along the ξ isoline and their exact values at each survey plane are interpolated from the adjacent fluid (edge) data. The surface gradients $\bar{\nabla} \cdot \mathbf{V}_e$ and $\bar{\nabla} \cdot \frac{1}{2}\mathbf{V}_e^2$ are not a direct output of the solver and the partial derivatives are therefore transformed in the more convenient local $s-n$ coordinate system instead:

$$\bar{\nabla} \cdot \mathbf{V}_e^2 \approx \frac{\partial V_e^2}{\partial s} \tag{B2}$$

where $\frac{\partial V_e^2}{\partial n} \approx 0$ and the evaluation of (B2) is then performed externally in MATLAB using a 2^{nd} order central difference scheme.

C. Summary of 2D Shear Layer Parameters and Identities

The paper makes extensive use of various shear layer parameters, defect quantities and identities which are summarized hereafter:

Volume-flux defect $\boldsymbol{Q}$ and volume-flux thickness $\boldsymbol{\delta}_k^*$:

$$\boldsymbol{Q} \equiv V_e \boldsymbol{\delta}_k^* \equiv \int_0^\delta (\boldsymbol{V}_e - \boldsymbol{V})\, dn \tag{C1}$$

Mass defect $\mathbf{M}$ and viscous displacement $\boldsymbol{\delta}^*$:

$$\mathbf{M} \equiv \rho_e V_e \boldsymbol{\delta}^* \equiv \int_0^\delta (\rho_e \boldsymbol{V}_e - \rho \boldsymbol{V})\, dn \tag{C2}$$

Density-flux defect $\mathbf{D}^{**}$ and density-flux thickness $\boldsymbol{\delta}^{**}$:

$$\mathbf{D}^{**} \equiv \rho_e V_e \boldsymbol{\delta}^{**} \equiv \int_0^\delta (\rho_e - \rho)\boldsymbol{V}\, dn \tag{C3}$$

Kinetic energy defect $\mathbf{K}^*$ and kinetic energy thickness $\boldsymbol{\theta}^*$:

$$\mathbf{K}^* \equiv^{**} \rho_e V_e^2 \boldsymbol{\theta}^* \equiv \int_0^\delta (V_e^2 - V^2)\rho \boldsymbol{V}\, dn \tag{C4}$$

Wake kinetic energy excess $\mathbf{K}$ and excess kinetic energy thickness $\boldsymbol{\kappa}$:

$$\mathbf{K} \equiv \rho_e V_e^2 \boldsymbol{\kappa} = \int_0^\delta (V_e - V)^2 \rho \boldsymbol{V}\, dn \tag{C5}$$

Density-flux thickness identity:

$$\boldsymbol{\delta}^{**} = \boldsymbol{\delta}^* - \boldsymbol{\delta}_k^* \tag{C6}$$

Density-flux defect identity:

$$\mathbf{D}^{**} = \mathbf{M} - \rho_e \boldsymbol{Q} \tag{C7}$$

Dissipation Integral $\mathcal{D}$:

$$\mathcal{D} \equiv \int_0^\delta (\bar{\bar{\tau}} \cdot \nabla) \cdot \boldsymbol{V}\, dn \tag{C8}$$

D. Volumetric Pressure Power of an Isentropic Streamtube

The 2nd Law of Thermodynamics for entropy generation is given by the Gibbs equation as [42]:

$$T\nabla s = \nabla e + p\nabla\frac{1}{\rho} \tag{D1}$$

where s and e the mass specific entropy and internal energy of the flow, respectively. Forming the dot product (D1)$\cdot\rho\boldsymbol{V}$ and invoking the quotient rule, the continuity relation $\nabla \cdot (\rho \boldsymbol{V}) = 0$ and vector expansion identities, the Gibbs equation obtains the equivalent form:

$$T\nabla \cdot (\rho\delta \mathrm{s}\boldsymbol{V}) - p_\infty \nabla \cdot \boldsymbol{V} = \nabla \cdot (\rho \delta e \boldsymbol{V}) + p_G \nabla \cdot \boldsymbol{V} \tag{D2}$$

where the additional substitutions $\delta s \rightarrow s - s_\infty$ and $\delta e \rightarrow e - e_\infty$ with respect to their free-stream values $()_\infty$, are permissible from continuity. Volume integration of (D2) alongside the Gauss' theorem (3) applied to an arbitrary isentropic streamtube, yields:

$$\Theta_\infty = \oiint (\rho \delta e \boldsymbol{V}) \cdot \hat{\boldsymbol{n}} \, d\mathcal{S} + p_\infty \oiint \boldsymbol{V} \cdot \hat{\boldsymbol{n}} \, d\mathcal{S} = 0 \tag{D3}$$

where contributions from the streamline side boundaries of the streamtube drop by definition due to flow tangency, $\boldsymbol{V} \cdot \hat{\boldsymbol{n}} = 0$ whereas contributions from the inlet/outlet flux surfaces lying in the freestream cancel out as equal and opposite. It follows that, the thermodynamic state of the fluid is reversibly restored and the net isentropic portion associated with the EIF reversibly goes to zero, such that $\Theta_\infty = \Theta_{r_\infty} = 0$.

E. Shock-induced Baroclinic Power Considerations

The defect formulations only account for viscous effects, however, the shock-related baroclinic loss component ($\mathcal{B}_{\text{shock}}$) can be implicitly incorporated. For that, consider the 2D flow scenarios of Fig. E1. The CV is chosen to be a streamtube that encloses the airfoil and extends sufficiently far from the airfoil such that it starts and ends at free-stream pressure.

Scenario a) corresponds to subsonic, adiabatic inviscid flow whose streamlines carry the same uniform total free-stream pressure at any streamwise position ($|\nabla P_t = 0|$), such that the flow field is isentropically restored downstream. From the Gibbs relation (D3), it follows that any isentropic compression and expansion result in $\mathcal{B}_\infty = 0$, in agreement with the expected zero drag power requirement (D'Alembert paradox).

Scenario b) corresponds to transonic, inviscid flow that triggers the formation of a shock on the body. A portion of the initially isentropic flow field crosses the shock wave region, resulting in a non-uniform drop of total pressure ($|\nabla P_t \neq 0|$) that translates to a shock wake downstream [42] and finite (wave) drag. Before and after the shock, the flow field is isentropic, meaning that the "violation" of isentropy within the examined streamtube occurs explicitly within the shock, such that the shock-induced baroclinic loss $\mathcal{B}_{\text{shock}}$ is spatially generated at the position of the shock. The above also correlate well with the exergy-based studies by Aguirre [35], who represents the shock loss (from an exergy perspective) as an anergy jump along the body.

The arguments of the Scenario b) may be effectively extended to the viscous transonic flow of Scenario c). The ambiguity however lies in the distinction between shock and boundary layer baroclinic losses, as this would require a clear distinction between shock and viscous domains. The two domains interact because the shock propagates within the boundary layer, such that a a part of the boundary layer after the shock carries additional losses from the shock, forming a shock-boundary layer mixing region.

To the extent that the shock wave can be adequately extracted from the numerical domain via an appropriate numerical filter, the boundary layer baroclinic loss $\mathcal{B}_{\text{BL}}$ may be directly estimated from its definition Eq. (29) and $\mathcal{B}_{\text{shock}}$

is implicitly estimated as:

$$\mathcal{B}_{\text{shock}} \simeq \mathcal{B}_{\infty} - \mathcal{B}_{\text{BL}} \tag{E1}$$

Notice that Eq. (E1) implies that the BL-shock mixing region is attributed to the boundary layer, even though a portion of it is a byproduct of the shock.

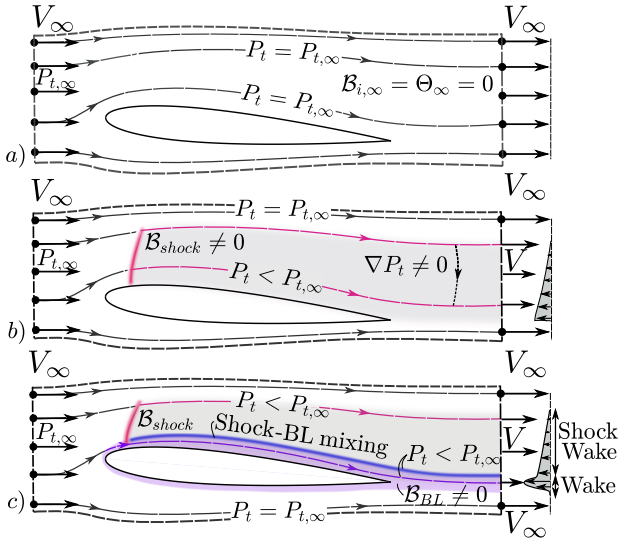


Fig. E1 Illustration of shock-induced baroclinic losses for a 2-D airfoil: a) Inviscid, subsonic flow. b) Inviscid, transonic flow with shock. c) Transonic viscous flow with shock.

Acknowledgments

The authors would like to express their gratitude to GKN Aerospace Services Limited for funding this research and for granting permission to publish the paper. The authors would additionally like to thank Joe Lister-Symonds for providing the NACA0012 CFD data sets. Finally, the pioneering work of Mark Drela is acknowledged as the main inspiration for the developed approach as well as the adoption of the notation and graphic styles used.

CRediT Author Contribution Statement

Ioannis Lamprakis: Conceptualisation, Methodology, Software, Validation, Formal Analysis, Data Curation, Writing - Original Draft, Writing - Review & Editing, Visualisation. **Drewan S. Sanders:** Conceptualisation, Review & Editing, Supervision.

References

[1] Oswatitsch, K., *Gas Dynamics*, 1st ed., Academic Press, New York, 1956, Chap. 4, pp. 207–210.

[2] Kusunose, K., *Drag prediction based on a wake-integral method*, 1998. https://doi.org/10.2514/6.1998-2723.

[3] Giles, M. B., and Cummings, R. M., "Wake integration for three-dimensional flowfield computations: Theoretical development," *Journal of Aircraft*, Vol. 36, No. 2, 1999. https://doi.org/10.2514/2.2465.

[4] Paparone, L., and Tognaccini, R., "Computational fluid dynamics-based drag prediction and decomposition," *AIAA Journal*, Vol. 41, No. 9, 2003. https://doi.org/10.2514/2.7300.

[5] Destarac, D., and Van Der Vooren, J., "Drag/thrust analysis of jet-propelled transonic transport aircraft; Definition of physical drag components," *Aerospace Science and Technology*, Vol. 8, No. 6, 2004. https://doi.org/10.1016/j.ast.2004.03.004.

[6] Kusunose, K., "A wake integration method for airplane drag prediction," *The 21st Century COE Program International COE of Flow Dynamics Lecture Series*, 2005.

[7] Maskell, E., "Progress towards a method for the measurement of the components of the drag of a wing of finite span," *RAE Technical Report No. 72232*, 1972.

[8] Van Dam, C. P., "Recent experience with different methods of drag prediction," *Progress in Aerospace Sciences*, Vol. 35, No. 8, 1999. https://doi.org/10.1016/S0376-0421(99)00009-3.

[9] Kroo, I., "Drag due to lift: Concepts for prediction and reduction," *Annual Review of Fluid Mechanics*, Vol. 33, 2001. https://doi.org/10.1146/annurev.fluid.33.1.587.

[10] Spalart, P. R., "On the far wake and induced drag of aircraft," *Journal of Fluid Mechanics*, Vol. 603, 2008. https://doi.org/10.1017/S0022112008001146.

[11] Wu, J.-Z., Ma, H.-Y., and Zhou, M.-D., "Vortical Aerodynamic Force and Moment," *Vorticity and Vortex Dynamics*, Springer, 2006, pp. 587–640.

[12] Marongiu, C., and Tognaccini, R., "Far-field analysis of the aerodynamic force by lamb vector integrals," *AIAA Journal*, Vol. 48, No. 11, 2010. https://doi.org/10.2514/1.J050326.

[13] Marongiu, C., Tognaccini, R., and Ueno, M., "Lift and lift-induced drag computation by lamb vector integration," *AIAA Journal*, Vol. 51, No. 6, 2013. https://doi.org/10.2514/1.J052104.

[14] Mele, B., Ostieri, M., and Tognaccini, R., "Vorticity based breakdown of the aerodynamic force in three-dimensional compressible flows," *AIAA Journal*, Vol. 54, No. 4, 2016. https://doi.org/10.2514/1.J054363.

[15] Kang, L. L., Russo, L., Tognaccini, R., Wu, J. Z., and Su, W. D., "Aerodynamic force breakdown in reversible and irreversible components by vortex force theory," *AIAA Journal*, Vol. 57, No. 11, 2019. https://doi.org/10.2514/1.J058379.

[16] Minervino, M., "A Unified Thermodynamic/Vortical Theory for the Aerodynamic Force Analysis," Ph.d. dissertation, University of Naples Federico II, Naples, Italy, February 2025.

[17] Drela, M., "Power Balance in Aerodynamic Flows," *AIAA Journal*, Vol. 47, No. 7, 2009, pp. 1761–1771. https://doi.org/10.2514/1.42409.

[18] Sanders, D. S., and Laskaridis, P., "Full-aircraft energy-based force decomposition applied to boundary-layer ingestion," *AIAA Journal*, Vol. 58, No. 10, 2020. https://doi.org/10.2514/1.J058695.

[19] Lamprakis, I., Sanders, D. S., and Laskaridis, P., "Fundamental Concepts of Boundary-Layer Ingestion Propulsion," *Journal of Aircraft*, published online 13 May 2025, pp. 1–22. https://doi.org/10.2514/1.C037675.

[20] Hall, D. K., Huang, A. C., Uranga, A., Greitzer, E. M., Drela, M., and Sato, S., "Boundary Layer Ingestion Propulsion Benefit for Transport Aircraft," *Journal of Propulsion and Power*, Vol. 33, No. 5, 2017, pp. 1118–1129. https://doi.org/10.2514/1.B36321.

[21] Lv, P., Ragni, D., Hartuc, T., Veldhuis, L., and Rao, A. G., "Experimental investigation of the flow mechanisms associated with a wake-ingesting propulsor," *AIAA Journal*, Vol. 55, No. 4, 2017. https://doi.org/10.2514/1.J055292.

[22] Uranga, A., Drela, M., Greitzer, E. M., Hall, D. K., Titchener, N. A., Lieu, M. K., Siu, N. M., Casses, C., Huang, A. C., Gatlin, G. M., and Hannon, J. A., "Boundary layer ingestion benefit of the D8 transport aircraft," *AIAA Journal*, Vol. 55, No. 11, 2017. https://doi.org/10.2514/1.J055755.

[23] Uranga, A., Drela, M., Hall, D. K., and Greitzer, E. M., "Analysis of the Aerodynamic Benefit from Boundary Layer Ingestion for Transport Aircraft," *AIAA Journal*, Vol. 56, No. 11, 2018. https://doi.org/10.2514/1.J056781.

[24] Della Corte, B., van Sluis, M., Veldhuis, L. L. M., and Gangoli Rao, A., "Power Balance Analysis Experiments on an Axisymmetric Fuselage with an Integrated Boundary-Layer-Ingesting Fan," *AIAA Journal*, Vol. 59, No. 12, 2021, pp. 5211–5224. https://doi.org/10.2514/1.J060570.

[25] Renard, N., and Deck, S., "A theoretical decomposition of mean skin friction generation into physical phenomena across the boundary layer," *Journal of Fluid Mechanics*, Vol. 790, No. 2016, 2016, pp. 339–367. https://doi.org/10.1017/jfm.2016.12.

[26] Sato, S., "The Power Balance Method For Aerodynamic Performance Assessment," Ph.d. dissertation, Massachusetts Institute of Technology, Cambridge, MA, June 2012.

[27] Drela, M., "Viscous Effects in Aerodynamic Flows," *Flight Vehicle Aerodynamics*, MIT Press, Cambridge, Massachusetts, 2014, Chap. 3, pp. 57–98.

[28] Drela, M., and Giles, M. B., "Viscous-inviscid analysis of transonic and low Reynolds number airfoils," *AIAA Journal*, Vol. 25, No. 10, 1987. https://doi.org/10.2514/3.9789.

[29] Drela, M., "XFOIL: an analysis and design system for low Reynolds number airfoils." *Low Reynolds Number Aerodynamics*, Vol. 54, edited by T.J. Mueller, No. Berlin, Germany, Springer-Verlag, 1989, pp. 1–12. https://doi.org/10.1007/978-3-642-84010-4_1.

[30] Fidkowski, K. J., "A Coupled Inviscid–Viscous Airfoil Analysis Solver, Revisited," *AIAA Journal*, Vol. 60, No. 5, 2022. https://doi.org/10.2514/1.J061341.

[31] Drela, M., "Boundary Layer Analysis," *Flight Vehicle Aerodynamics*, MIT Press, Cambridge, Massachusetts, 2014, Chap. 4, pp. 57–98.

[32] Méheut, M., and Bailly, D., "Drag-breakdown methods from wake measurements," *AIAA Journal*, Vol. 46, No. 4, 2008. https://doi.org/10.2514/1.29051.

[33] Schmitz, S., and Coder, J. G., "Inviscid circulatory-pressure field derived from the incompressible Navier-Stokes equations," *AIAA Journal*, Vol. 53, No. 1, 2015. https://doi.org/10.2514/1.J053140.

[34] Schmitz, S., "Drag decomposition using partial-pressure fields in the compressible Navier-Stokes equations," *AIAA Journal*, Vol. 57, No. 5, 2019. https://doi.org/10.2514/1.J057701.

[35] Aguirre, M., "Exergy Analysis of Innovative Aircraft with Aeropropulsive Coupling," Ph.d. dissertation, ISAE-University of Toulouse, Toulouse, France, February 2022.

[36] Aguirre, M. A., Duplaa, S., Carbonneau, X., and Turnbull, A., "Velocity decomposition method for exergy-based drag prediction," *AIAA Journal*, Vol. 58, No. 11, 2020. https://doi.org/10.2514/1.J059414.

[37] Arntz, A., "Civil aircraft aero-thermo-propulsive performance assessment by an exergy analysis of high-fidelity CFD-RANS Flow Solutions," Ph.D. thesis, Université de Lille 1, 2014.

[38] Arntz, A., Atinault, O., and Merlen, A., "Exergy-Based Formulation for Aircraft Aeropropulsive Performance Assessment: Theoretical Development," *AIAA Journal*, Vol. 53, No. 6, 2015, pp. 1627–1639. https://doi.org/10.2514/1.J053467.

[39] Mabey, D., "Effects of heat transfer on aerodynamics and possible implications for wind tunnel tests," *Progress in Aerospace Sciences*, Vol. 27, No. 4, 1990, pp. 267–303. https://doi.org/10.1016/0376-0421(90)90001-Z.

[40] Lamprakis, I., Sanders, D. S., and Laskaridis, P., "Energy-Based Aerodynamic Loss and Recovery Characteristics of Adiabatic and Heated Fuselages," *Journal of Aircraft*, Vol. 60, No. 6, 2023, pp. 1947–1964. https://doi.org/10.2514/1.C037246.

[41] Anderson Jr, J. D., " Turbulent Boundary Layers," *Fundamentals of aerodynamics*, McGraw-Hill Education in Aeronautical and Aerospace Engineering, New York, 2011, Chap. 19, 5th ed., pp. 550–599.

[42] Drela, M., "Physics of Aerodynamic Flows," *Flight Vehicle Aerodynamics*, MIT Press, Cambridge, Massachusetts, 2014, Chap. 1, pp. 1–21.

[43] Méheut, M., "Évaluation des composantes phénoménologiques de la traînée d'un avion à partir de résultats expérimentaux," Ph.d. dissertation, ONERA-Univ. of Sciences and Technologies of Lile, Lille, France, 2006.

[44] Moirou, N., Mutangara, N., and Sanders, D., "Fundamental considerations in the design and performance assessment of propulsive fuselage aircraft concepts," *The Aeronautical Journal*, 2024, p. 1–26. https://doi.org/10.1017/aer.2024.124.

[45] Celik, I. B., Ghia, U., Roache, P. J., Freitas, C. J., Coleman, H., and Raad, P. E., "Procedure for Estimation and Reporting of Uncertainty Due to Discretization in CFD Applications," *Journal of Fluids Engineering*, Vol. 130, No. 7, 2008, p. 078001. https://doi.org/10.1115/1.2960953.

[46] Jespersen, D. C., Pulliam, T. H., and Childs, M. L., "OVERFLOW Turbulence Modeling Resource Validation Results," Tech. rep., NASA Ames Research Center, Moffett Field, CA, 2016. URL https://turbmodels.larc.nasa.gov/Papers/NAS_Technical_Report_NAS-2016-01.pdf, nAS Technical Report NAS-2016-01.

[47] Lister-Symonds, J., "Power Balance Analysis of Adiabatic and Non-Adiabatic Aerofoils," Master's thesis, Cranfield University, Cranfield, UK, August 2021.

[48] Lister-Symonds, J., Ngonidzashe, M., Lamprakis, I., and Sanders, D., "Potential for Energy Recovery of a Non-Adiabatic Subsonic Airfoil," *Journal of Aircraft*, Accepted Manuscript, 2024.

[49] Lamprakis, I., "Energy-based Aerodynamic Principles of Adiabatic and Heated Boundary Layer Ingestion," Ph.d. dissertation, Cranfield University, England, UK, January 2023.

[50] Lamprakis, I., Sanders, D. S., and Laskaridis, "APROCONE WP1.1a Final Deliverable - Boundary Layer Ingestion Use Case," *Technical Report, APROCONE Project, UKRI Project Reference Number 113092*, April 2020.



https://dspace.org/

Defect force and viscous mechanical energy generation in aerodynamic flows

Lamprakis, Ioannis; Sanders, Drewan S.

2025-12-31
American Institute of Aeronautics and Astronautics (AIAA)
https://doi.org/10.2514/1.c037996
Lamprakis I, Sanders DS. (2025) Defect force and viscous mechanical energy generation in aerodynamic flows. Journal of Aircraft, Available online 26 November 2025

Downloaded from a DSpace repository. https://dspace.org/